

Thermodynamic topology optimization including plasticity

Miriam Kick, Philipp Junker

Leibniz University Hannover, Institute of Continuum Mechanics, Hannover, Germany

Corresponding author:

Philipp Junker, ✉ junker@ikm.uni-hannover.de

Abstract

In this contribution, we present an extension of the thermodynamic topology optimization that accounts for a non-linear material behavior due to the evolution of plastic strains. Physically, a plastic material behavior is characterized by a hysteresis in the stress/strain diagram after loading and unloading. In contrast, topology optimization is usually employed for a time-invariant load and the optimized component will only be loaded during physical use. Still, a virtual increase and decrease of strains, i. e. an unphysical evolution of the strains during the optimization process, is locally observed due to the evolution of the structure and thus modulation of the stiffness. If a classical plasticity model is employed for this unphysical “loading” and “unloading”, incorrect strain and stress states are computed due to the apparent energy dissipation and hysteresis in the stress/strain diagram. Therefore, this problem is usually resolved by recomputing the physical behavior for each optimization step: the initial conditions are refreshed by deleting all plastic strains computed for the previous optimization step. This restores the virgin state for the updated topology. The plastic strains are subsequently determined by evaluating the classical plasticity model which requires a discretization of the loading which results in several finite element simulations. After the correct plastic strains have been found, the next update step for the topology optimization is performed. To avoid this time-consuming procedure, we develop a novel surrogate material model that allows to correctly account for the physical state in terms of the plastic strains. Hence, finite element simulations purely for the plastic material behavior become obsolete such that the optimization of plastic materials now consumes comparable computation times as the optimization of elastic materials. The model is embedded into our strategy for topology optimization that routes back to thermodynamic extremal principles. Several numerical examples prove the capability of the novel surrogate material model.

1 Introduction

Engineers are always looking for structures that meet the specific requirements in an optimal way. One possibility for finding these structures is provided by optimization schemes which are classified as follows: i) improving the principal idea, ii) modifying the material, iii) thickness dimensioning, iv) optimization of shape and v) optimization of topology [33, 16]. Herein, the optimization scheme that demands the minimum amount of restrictions is given by topology optimization. There are various variants of topology optimization available as, e. g., the optimization for temperature evolution, noise reduction, dynamic response, or structural stiffness.

All of these approaches have in common that the related physical balance laws, in most cases the balance of linear momentum, are solved along with a mathematical optimization problem which is given in terms of an objective function. The most common objective is the minimization of compliance, i. e. the maximization of stiffness according to a target structure volume [34]. Therefore, topology optimization determines the position and arrangement of material within a given design space and boundary conditions such that the objective function is minimized. The topology of a structure can be parameterized via different approaches during the specific numerical investigation. For the numerical solution of the physical balance law, e. g., the balance of linear momentum, usually the finite element method (FEM) is employed. Consequently, the finite elements introduce a discretization of the design space and it is thus most common to assign a density value for each discrete subvolume, i. e. for each finite element. For this assignment, a variety of different numerical schemes has been developed among which the probably most popular is given by “Solid Material with Penalization (SIMP)” proposed by Bendsøe and Sigmund in [8, 9]. The fundamental idea of SIMP is the introduction of a non-linear interpolation function between void and full material such that a black and white design is aspired due to the inherent non-convex total potential. Further popular developments are overviewed in [34].

The consideration of the real materials properties offers additional potential for the optimal design of components. Therefore, it is important to account for the physical material behavior even during the process of topology optimization. In this context, the plastic material behavior plays a major role which requires a thermodynamically and mathematically rigorous treatment due to its complexity. In this field, Henryk Petryk has delivered important contributions: for instance, he proposed an approach based on incremental energy minimization in [28] and investigated thermodynamic stability conditions in [29]. Bifurcation problems have been analyzed in [32] and material modeling for complex loading paths in the context of finite deformations was presented in [31]. A textbook of Prof. Petryk on (in)stabilities including plastic solids is given in [30].

A direct access of plastic material behavior within topology optimization might be given by using classical plasticity models with the characteristic stress/strain diagram as given in Fig. 1. Several successful examples are provided in the literature: a first approach to account for a

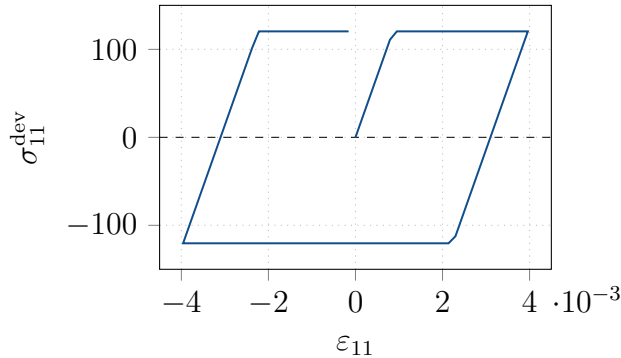


Figure 1: Classical elasto-plastic hysteresis curve

classical elasto-plastic material model within an adaptive material topology optimization was proposed by Maute *et al.* [26]. Approaches to determine plasticity by homogenization strategies are also possible, cf. [40]. This is particularly interesting for plastic parts of composites [35]. Furthermore, topology optimization based on finite strains can be considered for plasticity [37]. Nakshatralla and Tortorelli [27] optimize dynamically loaded structures while accounting for plastic material behavior. A different option was proposed by the consideration of damage, cf. [23, 5]. For all such non-linear stress/strain relations, the optimization routine usually demands

an additional algorithm for convergence. Here, one prominent possibility is provided by the “method of moving asymptotes” (MMA).

Unfortunately, the strategy of considering physical material models usually renders such optimization rather time-consuming: due to the local path-dependence, the physical loading process needs to be discretized with several time steps each of this demands the solution of the physical finite element problem. A prototype algorithm is given in Fig. 2. The nested

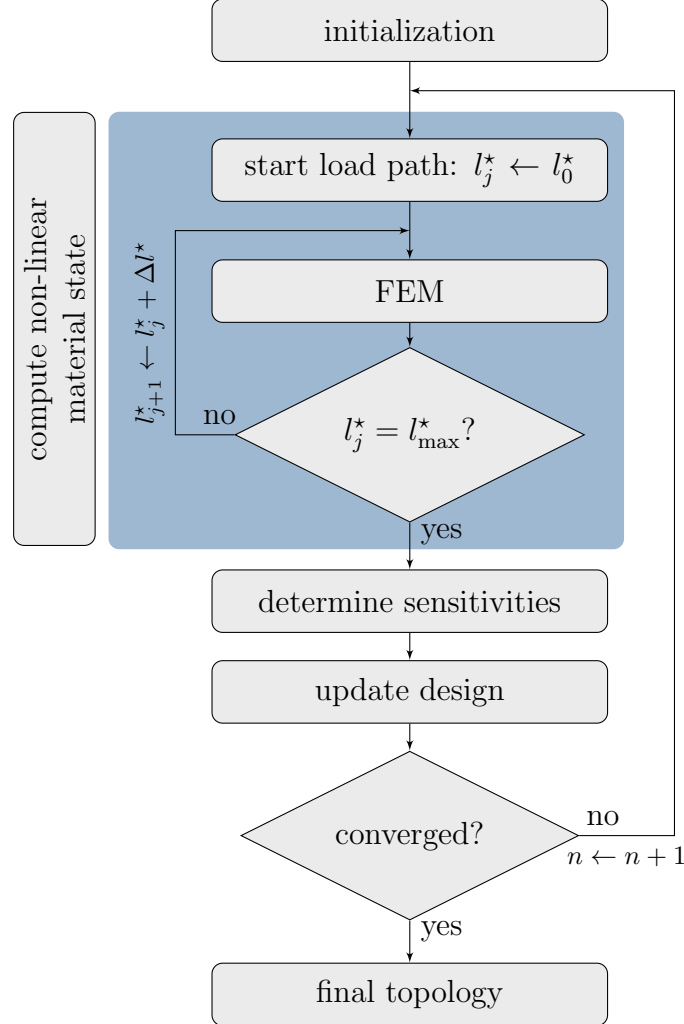


Figure 2: Strategy to account for non-linear material models during topology optimization

finite element simulation for the physical process and the topology optimization problem needs a remarkably higher amount of computation time. To compensate this drawback, several strategies can be found which aim to directly include plasticity into the optimization process: one approach is to couple an elastic model with local stress constraint as mentioned e.g. by [12, 13, 10, 25]. Another idea by Amir [6] is to define a single global stress constraint within the formulation of optimization problem to bypass the local calculation for each material point. Bruns *et al.* [11] propose to constrain the load-displacement by limit points in case of damage. Another way is to account for the nonlinear material behavior on a second, microscopic scale by developing a new model reduction technique which is proposed by Fritzen *et al.* [14] and extended by Xia *et al.* [39]. A special characteristic of this approach is the use of an evolutionary optimization method on the macroscopic scale. Furthermore, surrogate models have been developed which avoid the need of solving physical finite element problems. Zhao *et al.* [42, 41], for instance, developed a surrogate model as a fictitious non-linear elastic material model which asymptotically

approximates a perfect elasto-plastic behavior. They accounted for the von Mises criterion in [42] and also developed an approach valid for the Drucker-Prager criterion in [41]. Due to the absent path-dependence, the computation of the sensitivity is straight forward and only one finite element analysis needs to be computed for each iteration step. Unfortunately, this approach also has two significant disadvantages: first, the resulting stress/strain curve matches the similar classical elasto-plastic curve even at a material point level only at the limit points. Second, there is no possibility to compute the plastic strain tensor which serve as thermodynamic state variable. Third, remarkable differences in the stress field are detected when compared to the solutions with the “correct” elasto-plastic material model.

In order to improve the concept of surrogate models further, we propose a novel 3D surrogate material model which is not based on the idea of formulating a suitable hyperelastic free energy function to approximate the elasto-plastic material behavior. In contrast, we make use of the approach for classical modeling of plasticity and account for the hysteresis-free behavior by suppressing the dissipative character. Then, we obtain the advantage that we can match the results of plastic material models at the material point level, cf. Fig. 3. Furthermore, we are able to compute the physical state variable measured in terms of the plastic strain tensor. As will be shown by the numerical results, the stress distribution is computed with high accuracy.

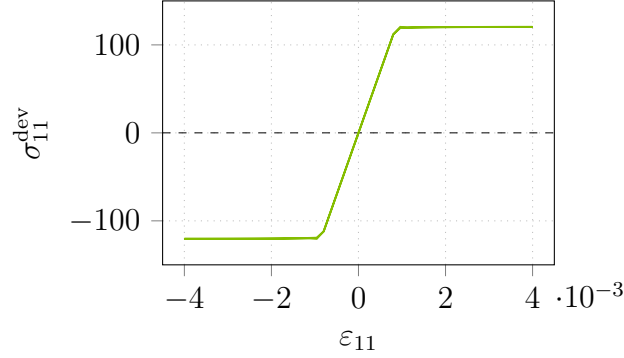


Figure 3: Simulated curve for the proposed surrogate material model

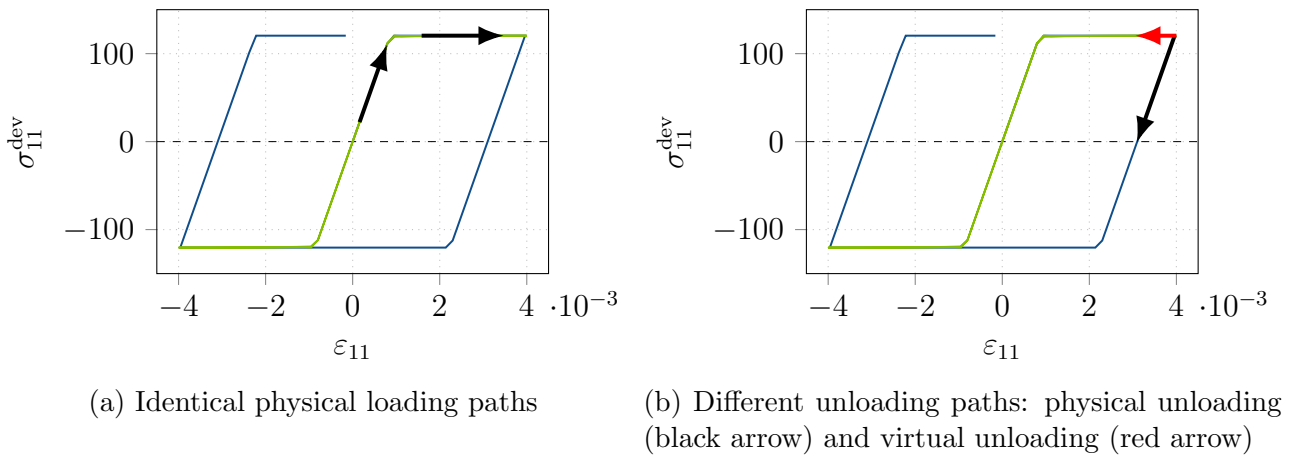


Figure 4: Comparison of the simulation results for loading and unloading: the result for a classical elasto-plastic model is given in blue; the result for the surrogate material is given in green

A schematic plot how our surrogate model works is provided in Fig. 4: the classical plasticity model results in the blue curves, yielding the well-known hysteresis. The green branch shows the result for the surrogate model. During loading, cf. Fig. 4a, both the classical and the surrogate

model yield the same stress/strain relation. However, both models behave remarkably different during unloading, cf. Fig. 4b: whereas the classical model shows a linear reduction of the stress, the stress in the surrogate model remains at the yield stress before linearly reducing in the elastic regime. It is worth to mentioning that the derivation of the surrogate model in 1D is trivial, but a challenging task for the 3D case since the stress is a tensor-valued tensor function. Once the surrogate model has been set, it provides huge advantages for the evolutionary optimization: here, the load state evolves while the topology evolves. For instance, high strains might be present in the beginning of the optimization process with associated high plastic strains. However, stiffness evolves during the optimization which might result in reduced strains and consequently plastic strains, see Fig. 5. The hysteresis-free character of the surrogate model allows to display this aspect directly, cf. Fig. 4b. The combination of this surrogate material model with a suitable numerical treatment, figured out in Fig. 6, allows to greatly reduce the total number of finite element simulations (cf. Fig. 2) while being physically accurate.

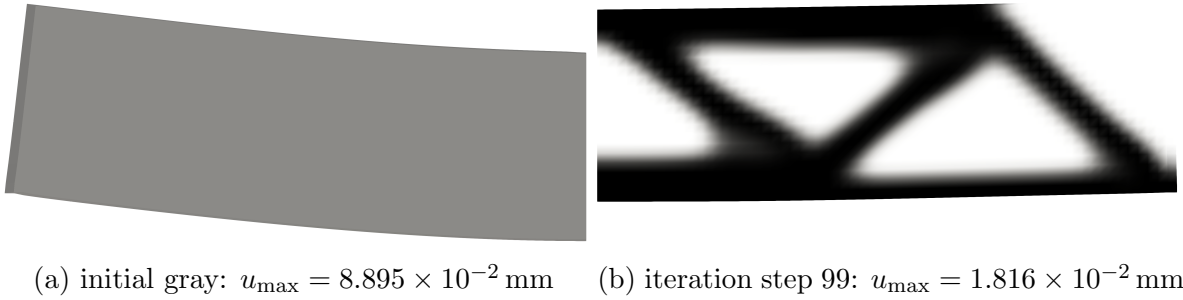


Figure 5: Evolution of stiffness and deformation (scaled with the factor 3) during evolution of topology for an elastic optimization

In a series of papers, we aimed at contributing to the problem of topology optimization: by using thermodynamic extremal principles, an evolutionary access to the problem of topology optimization has been presented for which we referred our method to as thermodynamic topology optimization (TTO). It routes back to [22] while further important developments have been presented for the numerical treatment in [17] and for hyperelastic material in [21]. This topology optimization makes use of an extended Hamilton principle which is well-known in the context of material modeling, cf. [20]. Therefore, the extended Hamilton functional is formulated and its stationarity conditions serve as update procedure for the evolution of the topology. In this manner, no classical optimization problem is formulated. Since the free energy function is part of the extended Hamilton functional, the result is very similar to classical schemes for topology optimization [18]. The manipulation of topology is managed by the density as state variable which is defined for each discretized area. One advantage of this thermodynamic topology optimization is that no further optimization algorithm is needed. In contrast, the relative density is described by a transient partial differential equation (PDE) in which the local free energy density serves as source term. Consequently, the material optimization problem is converted to an evolutionary problem. The field equation for the topology results from the stationary condition of the extended Hamilton functional. Additionally, evaluation of the functional results in the field equations for displacement and internal (state) variable which accounts for the (local) microstructure of the material. From this follows that the extended Hamilton functional according to topology optimization also features to take any physically dissipative material behavior into account. Therefore, a classical ideal plastic material model with the mentioned disadvantages of non-linearity and path-dependence could be derived. In this contribution, we aim at expanding the thermodynamic topology optimization such that it can be applied to elasto-plastic materials with the mentioned surrogate material model.

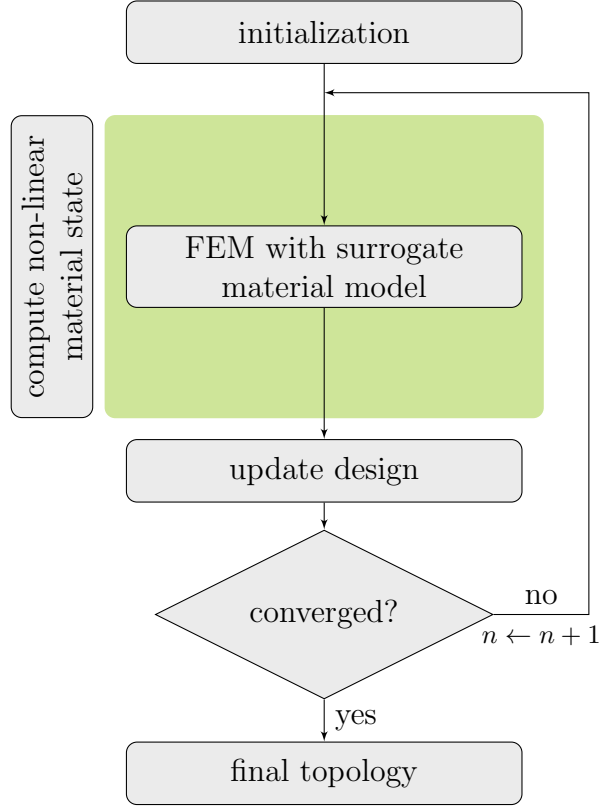


Figure 6: Strategy to account for non-linear material model with the proposed surrogate material model in thermodynamic topology optimization

This paper is structured as follows: first, we recall the basics of the thermodynamic topology optimization by use of Hamilton’s principle and complement our previous approaches by the inclusion of plasticity. To this end, we develop a surrogate material model for our topology optimization approach that accounts for plasticity without consideration of dissipation-related hysteresis effects. Afterwards we present a suitable strategy for numerical implementation. Then, the functionality of the proposed approach is tested and analyzed by means of computing topology optimizations for several boundary value problems.

2 Thermodynamic topology optimization including plasticity

The thermodynamic topology optimization is based on Hamilton’s principle which is usually a variational strategy for material modeling [20]. Assuming stationarity of an extended Hamilton functional follows the thermodynamic and physical laws and yields field equations for all state variables i.e. displacements, temperature and internal variables. Expanding the functional for topology optimization provides the benefit that the optimization problem can be tackled by a system of partial differential equations. Consequently, the mathematical optimization problem is converted into an evolutionary problem. At the same time, the stationarity of the extended Hamilton functional comprises the evolution of microstructural material behavior which affects the evolution of topology. Furthermore, constraints on the topology design as well as on the material behavior can be considered easily by taking use of Lagrange or Karush Kuhn Tucker parameters. It is worth mentioning that no classical optimization problem is solved in thermodynamic topology optimization. In contrast, the stationarity condition of the Hamilton functional

with respect to the density variable serves as update scheme for the topology.

We use the following notation for tensor operations: the single contraction is noted as “.” reading $\mathbf{a} \cdot \mathbf{b} = c \Leftrightarrow a_i b_i = c$ when applied to two vectors \mathbf{a} and \mathbf{b} , while it results in $\mathbf{A} \cdot \mathbf{b} = \mathbf{c} \Leftrightarrow A_{ij} b_j = c_i$ when applied to a vector and a second-order tensor \mathbf{A} . Moreover, the double contraction is denoted as “:”. It results in $\mathbf{A} : \mathbf{B} = c \Leftrightarrow A_{ij} B_{ij} = c$ when applied to two second-order tensors while it results in $\mathbb{A} : \mathbf{B} = \mathbf{C} \Leftrightarrow A_{ijkl} B_{kl} = C_{ij}$ when applied to a fourth-order tensor \mathbb{A} and a second-order tensor. Finally, the tensor product, i. e. the dyadic product, is noted as “ \otimes ” and reads $\mathbf{a} \otimes \mathbf{b} = \mathbf{C} \Leftrightarrow a_i b_j = C_{ij}$ when applied to two vectors and $\mathbf{A} \otimes \mathbf{B} = \mathbb{C} \Leftrightarrow A_{ij} B_{kl} = C_{ijkl}$ when applied to two second-order tensors.

In this contribution, the approach of topology optimization does not account for dynamic effects and therefore, we consider quasi-static loading. In this case, the extended Hamilton functional [20] for a quasi-static and isothermal case reads

$$(1) \quad \bar{\mathcal{H}} = \bar{\mathcal{H}}[\mathbf{u}, \mathbf{y}] := \mathcal{G}[\mathbf{u}, \mathbf{y}] + \mathcal{D}[\boldsymbol{\alpha}]$$

and sums the Gibbs energy \mathcal{G} and the dissipation-related work \mathcal{D} . This functional depends on the displacements \mathbf{u} and the state variable $\mathbf{y} = \{\boldsymbol{\alpha}, \chi\}$. The state variable is decomposed into the vectorial quantity $\boldsymbol{\alpha}$ collecting all internal variables which describe the physical material behavior in terms of the microstructural state, and the quantity χ as density variable for the topology optimization. Here, the density variable $\chi \in [\chi_{\min}, 1]$ with $\chi_{\min} > 0$ represents void “white” material for $\chi = \chi_{\min}$, the full “black” material for $\chi = 1$, and a mixed “gray” phase for $\chi \in]\chi_{\min}, 1[$. The relative density is then computed by $\rho = \rho(\chi)$ and $\rho(\chi) = \chi^3$, for instance. Here, we restrict ourselves to a single phase material, i. e. no multi-material optimization. An example for a multi-material optimization using the thermodynamic topology optimization has been presented in [15]. In our case of an elasto-plastic material, we thus chose $\boldsymbol{\alpha} = \boldsymbol{\varepsilon}^p$ where $\boldsymbol{\varepsilon}^p$ denotes the plastic part of the strain and $\boldsymbol{\varepsilon}^e$ the elastic part, i. e. $\boldsymbol{\varepsilon} = \boldsymbol{\varepsilon}^e + \boldsymbol{\varepsilon}^p$. According to Hamilton’s principle the stationary condition of the functional is provided as

$$(2) \quad \bar{\mathcal{H}} = \bar{\mathcal{H}}[\mathbf{u}, \boldsymbol{\varepsilon}^p, \chi] := \mathcal{G}[\mathbf{u}, \boldsymbol{\varepsilon}^p, \chi] + \mathcal{D}[\boldsymbol{\varepsilon}^p] \rightarrow_{\mathbf{u}, \boldsymbol{\varepsilon}^p, \chi} \text{stat} .$$

Therein, \mathcal{G} is defined as difference between the energy stored in the body with volume Ω and the work due to external forces. It hence reads

$$(3) \quad \mathcal{G}[\mathbf{u}, \boldsymbol{\varepsilon}^p, \chi] := \int_{\Omega} \Psi(\boldsymbol{\varepsilon}^e, \chi) \, dV - \int_{\Omega} \mathbf{b}^* \cdot \mathbf{u} \, dV - \int_{\Gamma_{\sigma}} \mathbf{t}^* \cdot \mathbf{u} \, dA$$

with the Helmholtz free energy Ψ , the body forces \mathbf{b}^* and the traction vector \mathbf{t}^* . The boundary conditions are defined as Dirichlet conditions for \mathbf{u}^* on Γ_u and as Neumann conditions for \mathbf{t}^* on Γ_{σ} . Hence, the complete boundary $\partial\Omega$ of the body is given by $\partial\Omega = \Gamma_u \cup \Gamma_{\sigma}$ and $\Gamma_u \cap \Gamma_{\sigma} = \emptyset$. Furthermore, the dissipation-related work is defined by

$$(4) \quad \mathcal{D} := \int_{\Omega} \mathbf{p}^{\text{diss}} : \boldsymbol{\varepsilon}^p \, dV$$

with the non-conservative force \mathbf{p}^{diss} which can be derived from the dissipation function Δ^{diss} by

$$(5) \quad \mathbf{p}^{\text{diss}} := \frac{\partial \Delta^{\text{diss}}}{\partial \boldsymbol{\varepsilon}^p} .$$

More details on the thermodynamic basis are provided in [20]. According to [21], the physically motivated Hamilton functional $\bar{\mathcal{H}}$ can be extended for thermodynamic topology optimization by adding

$$(6) \quad \mathcal{H}[\mathbf{u}, \boldsymbol{\varepsilon}^p, \chi] := \bar{\mathcal{H}}[\mathbf{u}, \boldsymbol{\varepsilon}^p, \chi] - \mathcal{R}[\chi] + \mathcal{C}[\boldsymbol{\varepsilon}^p, \chi] .$$

where additional constraints are included in \mathcal{C} and the rearrangement of topology is accounted for by the functional \mathcal{R} , defined as

$$(7) \quad \mathcal{R}[\chi] := \mathcal{D}_\chi[\chi] + \mathcal{F}[\chi] .$$

Here, the flux term

$$(8) \quad \mathcal{F}[\chi] := \int_{\Omega} \frac{1}{2} \beta \|\nabla \chi\|^2 \, dV$$

accounts for the convective rearrangement with the regularization parameter β . It thus serves as gradient penalization for the density variable and also controls the members size via the parameter β . Additionally, the source term

$$(9) \quad \mathcal{D}_\chi[\chi] := \int_{\Omega} p_\chi^{\text{diss}} \chi \, dV$$

accounts for local rearrangement. Analogously to (5), the non-conservative term for local rearrangement is assumed to be derivable from an associated dissipation function according to

$$(10) \quad p_\chi^{\text{diss}} := \frac{\partial \Delta_\chi^{\text{diss}}}{\partial \dot{\chi}} .$$

For the dissipation function, we follow [17] and chose

$$(11) \quad \Delta_\chi^{\text{diss}} = \frac{1}{2} \eta \dot{\chi}^2 .$$

The viscosity parameter η controls the velocity of evolution of topology. In this manner, the Hamilton functional (6) is able to couple microstructure evolution and topology optimization. We propose that an optimal structure can be found if this functional becomes stationary.

The stationary condition with respect to all variables

$$(12) \quad \delta \mathcal{H} = \delta_{\mathbf{u}} \mathcal{H} + \delta_{\boldsymbol{\varepsilon}^p} \mathcal{H} + \delta_\chi \mathcal{H} = 0 \quad \forall \delta_{\mathbf{u}}, \delta_{\boldsymbol{\varepsilon}^p}, \delta_\chi$$

yields the following system of governing equations

$$(13) \quad \begin{cases} \delta_{\mathbf{u}} \mathcal{H} = 0 = \int_{\Omega} \frac{\partial \Psi}{\partial \boldsymbol{\varepsilon}} : \delta \boldsymbol{\varepsilon} \, dV - \int_{\Omega} \mathbf{b}^* \cdot \delta \mathbf{u} \, dV - \int_{\Gamma_\sigma} \mathbf{t}^* \cdot \delta \mathbf{u} \, dA & \forall \delta \mathbf{u} \\ \delta_{\boldsymbol{\varepsilon}^p} \mathcal{H} = 0 = \int_{\Omega} \frac{\partial \Psi}{\partial \boldsymbol{\varepsilon}^p} : \delta \boldsymbol{\varepsilon}^p \, dV + \int_{\Omega} \frac{\partial \Delta^{\text{diss}}}{\partial \dot{\boldsymbol{\varepsilon}}^p} : \delta \dot{\boldsymbol{\varepsilon}}^p \, dV + \delta_{\boldsymbol{\varepsilon}^p} \mathcal{C} & \forall \delta \boldsymbol{\varepsilon}^p \\ \delta_\chi \mathcal{H} = 0 = \int_{\Omega} \frac{\partial \Psi}{\partial \chi} \delta \chi \, dV - \int_{\Omega} \eta \dot{\chi} \delta \chi \, dV - \int_{\Omega} \beta \nabla \chi \cdot \nabla \delta \chi \, dV + \delta_\chi \mathcal{C} & \forall \delta \chi \end{cases}$$

where each equation belongs to one of the independent system variables, cf. also [21] for a general microstructure consideration in case of finite deformations. Here, the standard notation $\delta \boldsymbol{\varepsilon} := \text{sym}(\nabla \otimes \delta \mathbf{u})$ is used. The first condition is identified as the weak form of the balance of the linear momentum where the stress is given by $\boldsymbol{\sigma} = \partial \Psi / \partial \boldsymbol{\varepsilon}$. The second condition constitutes as governing equation for the plastic strains $\boldsymbol{\varepsilon}^p$ and the last equation is the field equation for topology optimization.

Remark: the surrogate model is based on the same principles as used for usual material modeling. This is a fundamentally different approach as, for instance, defining hyperelastic stress/strain relations. Here, of course, the elasto-plastic material behavior might be approximated in the 1D case and the related model becomes trivial. However, when dealing with the

3D case, the stress/strain relation is a tensor-valued tensor function: both the function, i.e. the stress, as well as the variable, i.e. the strain, are tensor-valued. The construction of appropriate relations is a high-dimensional task which is far from being trivial. We thus make use of established strategies for material modeling and adapt them accordingly for the optimization process. The introduction of plastic strains significantly simplifies the entire procedure since the stress state is uniquely defined once the (total) strain and its plastic part are determined.

2.1 Specification of the energetic quantities

The model is completed by specifications of the free energy density Ψ , the dissipation function Δ^{diss} , and the constraint functional \mathcal{C} . For the free energy, we follow the classical approach of elasto-plastic materials and combine it with the SIMP approach for the relative density. This gives

$$(14) \quad \Psi(\boldsymbol{\varepsilon}^e, \chi) = \rho(\chi) \Psi_0 := \frac{1}{2} (\boldsymbol{\varepsilon} - \boldsymbol{\varepsilon}^p) : \chi^3 \mathbb{E}_0 : (\boldsymbol{\varepsilon} - \boldsymbol{\varepsilon}^p)$$

where the stiffness tensor of the full material is given by \mathbb{E}_0 and the energy of the virtually full material is given by $\Psi_0 := (\boldsymbol{\varepsilon} - \boldsymbol{\varepsilon}^p) : \mathbb{E}_0 : (\boldsymbol{\varepsilon} - \boldsymbol{\varepsilon}^p)/2$. We use $\rho(\chi) = \chi^3$ for the density where other approaches are also possible, see [21] where a sigmoid function has been used. Consequently, we obtain for the stresses

$$(15) \quad \boldsymbol{\sigma} = \frac{\partial \Psi}{\partial \boldsymbol{\varepsilon}} = \chi^3 \mathbb{E}_0 : (\boldsymbol{\varepsilon} - \boldsymbol{\varepsilon}^p) .$$

The derivative of Ψ with respect to $\boldsymbol{\varepsilon}^p$ thus yields

$$(16) \quad \frac{\partial \Psi}{\partial \boldsymbol{\varepsilon}^p} = -\boldsymbol{\sigma}$$

and the derivative of Ψ with respect to χ yields

$$(17) \quad p := -\frac{\partial \Psi}{\partial \chi} = -3\chi^2 \Psi_0 .$$

It is worth mentioning that $\chi > \chi_{\min}$. Consequently, the driving force p is non-zero for all conditions with $\Psi_0 \neq 0$. Furthermore, the evolution of plastic strains influences Ψ_0 and, in turn, the driving force p and thus the update condition for optimization, cf. (13)₃. In a classical elasto-plastic material model, the dissipation function is defined as

$$(18) \quad \Delta^{\text{diss}} = r \|\dot{\boldsymbol{\varepsilon}}^p\|$$

with the yield limit r . This approach yields a rate-independent formulation. Details on such an approach can be found, e.g., in [19, 20]. However, this physically motivated choice would contradict our intention to prevent the path-dependence and the related dissipative material behavior. Therefore, we formulate the surrogate material model for the evolution of plastic strains in the context of thermodynamic topology optimization regarding the following assumptions: i) the dissipation-free evolution is acquired by postulating a vanishing dissipation function, i.e. $\Delta^{\text{diss}} = 0$; ii) the yield condition is included by demanding

$$(19) \quad \|\boldsymbol{\sigma}^{\text{dev}}\| = r$$

during plastic evolution where the stress deviator $\boldsymbol{\sigma}^{\text{dev}} = \boldsymbol{\sigma} - 1/3 \text{tr } \boldsymbol{\sigma} \mathbf{I}$ is computed by

$$(20) \quad \boldsymbol{\sigma}^{\text{dev}} = \mathbb{P} : \boldsymbol{\sigma}$$

with the projection tensor \mathbb{P} ; and iii) the plastic strains are volume-preserving, i. e.

$$(21) \quad \text{tr } \boldsymbol{\varepsilon}^p = 0 \Leftrightarrow \boldsymbol{\varepsilon}^p : \mathbf{I} = 0 .$$

The limitation of stress and the volume preservation are included through the constraint functional by using the Lagrange parameters λ_σ and λ_V , respectively. Hardening can be included by choosing a non-constant threshold value $r = r(\|\boldsymbol{\varepsilon}^p\|)$ which is postponed to future works.

It remains to identify the constraints for the density variable χ to finally formulate the constraint functional \mathcal{C} . The first constraint is given by the interval in which χ is defined: values of χ that are negative are not reasonable; same limitation holds true for values of χ that are larger than one. Consequently, we demand $\chi \in [\chi_{\min}, 1]$ where the lower bound is set to a small value $\chi_{\min} > 0$ due to numerical reasons. These bounds are taken into account by use of a Karush Kuhn Tucker parameter γ . Furthermore, the volume of the topology relative to the total design volume is prescribed by the parameter ϱ_0 . Consequently, it has to hold

$$(22) \quad \int_{\Omega} \chi \, dV = \varrho_0 \Omega$$

which is included to the constraint functional by use of a Lagrange parameter λ_χ .

Combining these four constraints, i. e. norm of the stress deviator being equivalent to the yield stress, volume preservation of the plastic strains, bounded interval for χ , and control of the total mass, we finally arrive at

$$(23) \quad \mathcal{C} := \lambda_\sigma \int_{\Omega} (\|\boldsymbol{\sigma}^{\text{dev}}\| - r) \, dV + \lambda_V \int_{\Omega} \mathbf{I} : \boldsymbol{\varepsilon}^p \, dV + \int_{\Omega} \gamma \chi \, dV + \lambda_\chi \left(\int_{\Omega} \chi \, dV - \varrho_0 \Omega \right) .$$

2.2 The stationarity condition with respect to the plastic strains

It remains to appropriately analyze the stationarity condition of the Hamilton functional with respect to the plastic strains. This conditions enables us to compute the plastic strains which, in combination with the total strain, specify the stress state. To this end, we use the specifications for a vanishing dissipation function Δ^{diss} and the constraint functional (23) to evaluate (13)₂ as

$$(24) \quad \begin{aligned} & \int_{\Omega} \left(-\boldsymbol{\sigma} + \lambda_\sigma \frac{\partial \|\boldsymbol{\sigma}^{\text{dev}}\|}{\partial \boldsymbol{\varepsilon}^p} + \lambda_V \mathbf{I} \right) : \delta \boldsymbol{\varepsilon}^p \, dV = 0 \quad \forall \delta \boldsymbol{\varepsilon}^p \\ \Rightarrow \quad & \boldsymbol{\sigma} = \lambda_\sigma \frac{\partial \|\boldsymbol{\sigma}^{\text{dev}}\|}{\partial \boldsymbol{\varepsilon}^p} + \lambda_V \mathbf{I} = -\lambda_\sigma \frac{\boldsymbol{\sigma}^{\text{dev}}}{\|\boldsymbol{\sigma}^{\text{dev}}\|} : \mathbb{P} : \chi^3 \mathbb{E}_0 + \lambda_V \mathbf{I} . \end{aligned}$$

Solving (24) for the plastic strains constitutes our surrogate model for the plastic material behavior. A detailed derivation of the Lagrange multipliers is deferred to App. A. There, we show that the governing equation for the plastic strains is given as

$$(25) \quad \mathbb{P} : \left(-\boldsymbol{\sigma} + \frac{r^2}{\boldsymbol{\sigma}^{\text{dev}} : \mathbb{E}_0 : \boldsymbol{\sigma}^{\text{dev}}} \boldsymbol{\sigma}^{\text{dev}} : \mathbb{E}_0 \right) = \mathbf{0}$$

which is a non-linear algebraic equation.

Remark: it is worth mentioning that we do not receive a differential equation for the internal variable as it is usually the case. This routes back to assuming a dissipation-free evolution of the plastic strains which, in turn, are determined by energy minimization.

Remark: the equation for determining the plastic strains in (25) can be interpreted in the way that the tensor

$$(26) \quad \mathbf{s} := -\boldsymbol{\sigma} + \frac{r^2}{\boldsymbol{\sigma}^{\text{dev}} : \mathbb{E}_0 : \boldsymbol{\sigma}^{\text{dev}}} \boldsymbol{\sigma}^{\text{dev}} : \mathbb{E}_0$$

is projected onto the deviator subspace by $\mathbb{P} : \mathbf{s}$. Consequently, all quantities \mathbf{s} whose projection onto the deviator subspace equal the zero tensor solve (26), i.e., $\mathbb{P} : \mathbf{s}$ may be solved both by deviatoric and non-deviatoric \mathbf{s} , for instance, which indicates that no unique solution exists. We therefore employ a special numerical solution strategy for selecting an appropriate solution. We discuss the numerical treatment in Sec. 3.2.

Components of the plastic strain tensor only evolve to compensate stresses with a deviator norm greater than the yield stress. Therefore, it is mandatory to identify a suitable criterion for distinguishing whether an elastic or plastic material behavior is present. Since the purpose of the modified surrogate plasticity model is to display the same material behavior for loading like a classical material model for elasto-plasticity, we make use of the indicator function that would result from the dissipation function in (18) via a Legendre transformation, cf. [19]. This indicator function reads

$$(27) \quad \Phi = \|\boldsymbol{\sigma}^{\text{dev}}\| - r \leq 0$$

where elastic behavior is present for $\Phi < 0$ and plastic behavior for $\Phi = 0$ with the deviator norm of the yield stress r .

Remark: It is worth mentioning that it is not possible to determine the plastic strains from the condition $\Phi = 0$: this is a scalar-valued condition which does not provide sufficient information for the computation of the six individual components of the symmetric tensor-valued plastic strain $\boldsymbol{\varepsilon}^p$.

Fitting the characteristic of the classical elasto-plastic material model, physical unloading from a plastic state can be detected by this indicator function when the stress decreases once again below the yield stress. The elastically stored energy is released first and the residual, plastic strain remains. In this way, the hysteresis loop in the stress/strain diagram of a physical material evolves. This behavior must be suppressed by the surrogate material model as discussed above. Thus, the stress is not a suitable measure for the indicator function related to the surrogate model.

For the proposed surrogate material model in the context of optimization, however, only the agreement of a physically correct loading curve is demanded – the unloading process must not correspond to the physical evolution of plastic strains: it occurs in topology optimization only due to virtual changes of the structure stiffness which are uncorrelated to physical unloading. Due to this reason, a vanishing dissipation function is defined to “suppress” the unloading part of the hysteresis curve to achieve a dissipation-free, virtual unloading valid in the optimization process. Virtual unloading from a plastic state should result in a decrease of plastic strains. Thus, the plastic strain is reduced first and only if no plastic strains are present anymore, the elastically stored energy is released. In this way, the loading branch in the stress/strain curve is followed both for loading and virtual unloading due to stiffness evolution. Consequently, we need to reformulate the indicator function (27) in terms of strains. We defer the detailed derivation to App. B and present here the result which is the yield function as function of strains

$$(28) \quad \Phi(\boldsymbol{\varepsilon}) := \|\boldsymbol{\varepsilon}\| - \varepsilon_{\text{exp}}^Y \quad \text{where} \quad \Phi = \begin{cases} < 0 & \text{elastic} \\ \geq 0 & \text{plastic} \end{cases}.$$

The yield limit in terms of an equivalent strain measure is given as

$$(29) \quad \varepsilon_{\text{exp}}^Y = \frac{r}{\|\mathbb{P} : \chi^3 \mathbb{E}_0 : \tilde{\boldsymbol{\varepsilon}}_{\text{tens}}\|} = \sqrt{\frac{2}{3}} \frac{\sigma_{\text{exp}}^Y}{\|\mathbb{P} : \chi^3 \mathbb{E}_0 : \tilde{\boldsymbol{\varepsilon}}_{\text{tens}}\|}$$

2.3 The stationarity condition with respect to the density variable

Finally, the evolution of the density variable needs to be formulated. Therefore, it remains to investigate the governing equation for the density variable χ which is given by (13)₃. Making use of the constraint functional \mathcal{C} in (23) and the driving force for topology optimization p in (17), the stationarity with respect to χ takes the form

$$(30) \quad \int_{\Omega} (-p - \eta \dot{\chi} + \gamma + \lambda_{\chi}) \delta\chi \, dV - \int_{\Omega} \beta \nabla \chi \cdot \nabla \delta\chi \, dV = 0 \quad \forall \delta\chi$$

which is a parabolic differential equation and shows some similarities to phase field equations, cf. [7] for instance. Analogously to the stationarity with respect to the displacements in (13)₁, this equation (30) is the weak form of the associated Euler equation (which is the balance of linear momentum for the displacements). Therefore, one possibility for numerical evaluation would be given by direct application of the finite element method. A comparable approach has been presented in [22]. However, it has turned out that this procedure is much more time consuming than applying the numerical method that has been presented in [17] due to the complex constraints of the bounded interval for χ and the prescribed total density ϱ_0 . Therefore, in order to apply the method of the previous work in [17] which reduces the numerical efforts by approximately one order of magnitude, we transform (30) to its strong form by integration by parts. This results in

$$(31) \quad \begin{cases} \eta \dot{\chi} = -p + \beta \Delta \chi + \lambda_{\chi} + \gamma & \forall \mathbf{x} \in \Omega \\ \mathbf{n} \cdot \nabla \chi = 0 & \forall \mathbf{x} \in \partial\Omega \end{cases}$$

where (31)₂ is the Neumann boundary condition for the density variable. It ensures conservation of the prescribed total structure volume. Meanwhile, the change of the density variable is defined by (31)₁ and accounts for the Laplace operator which is defined as $\Delta \chi := \partial^2 \chi / \partial x^2 + \partial^2 \chi / \partial y^2 + \partial^2 \chi / \partial z^2$. The transient characteristic of this term require the specification of an initial value for $\chi(\mathbf{x}, t = 0) = \chi^{\text{ini}} \forall \mathbf{x} \in \Omega$, which will be introduced with the numerical treatment in Sec. 3.3.

3 Numerical implementation

In summary, the following system of coupled differential-algebraic equations needs to be solved:

$$(32) \quad \begin{cases} 0 = \int_{\Omega} \boldsymbol{\sigma} \cdot \delta \boldsymbol{\varepsilon} \, dV - \int_{\Omega} \mathbf{b}^* \cdot \delta \mathbf{u} \, dV - \int_{\partial\Omega} \mathbf{t}^* \cdot \delta \mathbf{u} \, dA & \forall \delta \mathbf{u} \\ \mathbf{0} = \mathbb{P} \cdot \mathbf{s} & \forall \mathbf{x} \in \Omega \\ \dot{\chi} = \frac{1}{\eta} (-p + \beta \Delta \chi + \lambda_{\chi} + \gamma) & \forall \mathbf{x} \in \Omega \end{cases}$$

It is worth mentioning that we use for now on the usual Voigt notation for the stresses and strains which reduces, for instance, the double contraction to a scalar product in (32)₁ and (32)₂. The equations (32) have to be solved numerically for the displacement field \mathbf{u} , the microstructural plastic strain $\boldsymbol{\varepsilon}^p$ and the topology density χ .

The governing equation for the density variable in (32)₃ includes a transient term, indicated by $\dot{\chi}$. This term allows for an evolutionary update of the density field and stabilizes the numerical treatment. To this end, the interpretation of the time derivative is slightly different as for other field equations that contain transient terms, as, e. g., the heat conduction equation: in our case

of thermodynamic topology optimization, the pseudo-time corresponds to an update step during the iterative solution of (32). However, we employ a standard discretization in pseudo-time, given as

$$(33) \quad \Delta t := t_{n+1} - t_n$$

where t_{n+1} refers to the current iteration step and t_n to the previous iteration step.

The numerical solution of the system of equations in (32) is a sophisticated task due to the inherent non-linearities, constraints, and strong coupling. Therefore, instead of applying a monolithic update scheme, cf. [22], we solve the equations in a staggered manner. This can be interpreted as operator split which has turned beneficial in our previous works as in [17] and also for adaptive finite element usage in [36].

3.1 The update of the displacements

Due to the operator split, a standard finite element approach is employed for updating the displacements and the stress in $(32)_1$ is evaluated as

$$(34) \quad \boldsymbol{\sigma}_{n+1} = \chi_n^3 \mathbb{E}_0 \cdot (\boldsymbol{\varepsilon}_{n+1} - \boldsymbol{\varepsilon}_n^p)$$

To this end, the displacement field is approximated using the Galerkin-Ansatz

$$(35) \quad u_k = N_o u_o^{(k)} = \mathbf{N} \cdot \hat{\mathbf{u}}^{(k)}$$

with the shape function \mathbf{N} and the nodal displacement $\hat{\mathbf{u}}^{(k)}$ in the spatial direction k . Therefore, the weak form of the balance of linear momentum in $(32)_1$ transforms to

$$(36) \quad \int_{\Omega} \boldsymbol{\sigma} \cdot \delta \boldsymbol{\varepsilon} \, dV = \delta \hat{\mathbf{u}} \cdot \int_{\Omega} \mathbf{B}^T \cdot \boldsymbol{\sigma} \, dV = 0 =: \delta \hat{\mathbf{u}} \cdot \mathbf{r} \quad \forall \delta \hat{\mathbf{u}}$$

when body forces are neglected. Here, \mathbf{B} denotes the usual operator matrix including the spatial derivatives of the shape function. The quantity $\delta \hat{\mathbf{u}}$ is the global column matrix of nodal virtual displacements which also includes the Dirichlet boundary conditions. Finally, the global residual column matrix is denoted by \mathbf{r} and, accordingly, the nodal displacements will be found from $\mathbf{r} = \mathbf{0}$. The global residual \mathbf{r} is assembled in usual manner by

$$(37) \quad \mathbf{r} := \mathbf{A}_e \mathbf{r}_e \quad \text{where} \quad \mathbf{r}_e := \int_{\Omega_e} \mathbf{B}_e^T \cdot \boldsymbol{\sigma} \, dV$$

denotes the residual column matrix for each element e . More details on the finite element method can be found in standard textbooks, e. g., [38].

Remark: The thermodynamic topology optimization including plasticity has been numerically coded in the programming language Julia [2] where we made use of the finite element toolbox Ferrite (previous called JuAFEM) [1].

Ferrite uses a gradient-based equation solver as it is the standard for many finite element programs. Consequently, the iterative solution process for $\mathbf{r} = \mathbf{0}$ is performed by

$$(38) \quad \mathbf{r}^{i+1} = \mathbf{r}^i + \frac{\partial \mathbf{r}}{\partial \hat{\mathbf{u}}} \cdot \Delta \hat{\mathbf{u}} = \mathbf{0}$$

where the iteration number is given by i . The increment $\Delta \hat{\mathbf{u}}$ updates the displacement field iteratively for fixated plastic strains $\boldsymbol{\varepsilon}_n^p$ and density field χ_n . The required element tangent is computed as

$$(39) \quad \frac{\partial \mathbf{r}_e}{\partial \hat{\mathbf{u}}_e} = \int_{\Omega_e} \mathbf{B}_e^T \cdot \chi_n^3 \mathbb{E}_0 \cdot \mathbf{B}_e \, dV$$

with the column matrix of displacements for each finite element e denoted as $\hat{\mathbf{u}}_e$. Then, the assembled tangent is constructed by

$$(40) \quad \frac{\partial \mathbf{r}}{\partial \hat{\mathbf{u}}} = \mathbf{A}_e \frac{\partial \mathbf{r}_e}{\partial \hat{\mathbf{u}}_e}.$$

Remark: It is worth mentioning that we used the tensors package [4] of Julia in our numerical implementation which is optimized for using tensors of higher order. Therefore, we did not perform a finite element programming in standard form, i.e., by using the Voigt notation, but used the full tensor notation. This, of course, also effects the dimensions of the other quantities, i.e., the \mathbf{B} operator is an array with three indices. For a more usual presentation, we presented the formulas by using the Voigt notation and deferred our array-based programming using the tensors package to App. C.

3.2 The update of the plastic strains

The plastic strain is defined, as usual, for each integration point. According to the discretization we employ for the density variable, all integration points in the same finite element e are evaluated with the same value for the density variable χ_e . More details are given later when we discuss the numerical treatment for the density variable.

The plastic strains are determined from solving $(32)_2$ which is a non-linear algebraic equation. As already indicated, the projection of \mathbf{s} onto its deviator subspace prevents existence of a unique solution of $(32)_2$ for the plastic strains: the kernel of \mathbb{P} defines the solution space. A result of this ill-posed problem is that numerical strategies to directly solve $\mathbb{P} \cdot \mathbf{s} = \mathbf{0}$ fail, for instance due to a singular tangent matrix in a Newton scheme. This can be seen when analyzing the deviator operator in more detail. It is given in Voigt notation by

$$(41) \quad \mathbb{P} = \begin{pmatrix} \frac{2}{3} & -\frac{1}{3} & -\frac{1}{3} & 0 & 0 & 0 \\ -\frac{1}{3} & \frac{2}{3} & -\frac{1}{3} & 0 & 0 & 0 \\ -\frac{1}{3} & -\frac{1}{3} & \frac{2}{3} & 0 & 0 & 0 \\ 0 & 0 & 0 & 1 & 0 & 0 \\ 0 & 0 & 0 & 0 & 1 & 0 \\ 0 & 0 & 0 & 0 & 0 & 1 \end{pmatrix}$$

and has the eigensystem (eigenvector \mathbf{v} & related eigenvalue κ)

$$(42) \quad \begin{aligned} \mathbf{v}_1 &= (0 \ 0 \ 0 \ 0 \ 0 \ 1) & : \ \kappa_1 &= 1 \\ \mathbf{v}_2 &= (0 \ 0 \ 0 \ 0 \ 1 \ 0) & : \ \kappa_2 &= 1 \\ \mathbf{v}_3 &= (0 \ 0 \ 0 \ 1 \ 0 \ 0) & : \ \kappa_3 &= 1 \\ \mathbf{v}_4 &= (-1 \ 0 \ 1 \ 0 \ 0 \ 0) & : \ \kappa_4 &= 1 \\ \mathbf{v}_5 &= (-1 \ 1 \ 0 \ 0 \ 0 \ 0) & : \ \kappa_5 &= 1 \\ \mathbf{v}_6 &= (1 \ 1 \ 1 \ 0 \ 0 \ 0) & : \ \kappa_6 &= 0 \end{aligned}$$

from which we recognize that a solution to $\mathbb{P} \cdot \mathbf{s} = \mathbf{0}$ is given by all vectors \mathbf{s} that have identical structure like \mathbf{v}_6 which is related to eigenvalue $\kappa_6 = 0$, i.e.

$$(43) \quad \mathbf{s} = (\zeta \ \zeta \ \zeta \ 0 \ 0 \ 0)$$

solves $(32)_2$ for arbitrary values of $\zeta \in \mathbb{R}$. It is thus necessary to specify the value ζ to compute the update of the plastic strains. For now, we make a most intuitive guess and set $\zeta = 0$ which

allows for a unique solution. This transforms the originally ill-posed mathematical problem to a well-posed one. From (43), we recognize that \mathbf{s} has the structure of a hydrostatic pressure and it is thus convenient to solve $\mathbf{s} = \mathbf{0}$ in the eigenspace. Consequently, the numerical update of the plastic strains starts with applying a coordinate transformation of the equation (32)₂ into the eigenspace. The transformation is performed by means of the transformation matrix \mathbf{T} which collects the three vectors for the eigen directions. It is obtained by applying the eigensystem routine of Julia [2]. In the eigenspace, the strain and stress tensors reduce to vectors with three components. We denote this vector by $\tilde{\boldsymbol{\varepsilon}}$ and $\tilde{\boldsymbol{\sigma}}$, respectively, where the components of the strain in the eigenspace are given as

$$(44) \quad \tilde{\varepsilon}_i = (\mathbf{T}^T \cdot \boldsymbol{\varepsilon} \cdot \mathbf{T})_{ii} \quad (\text{no summation over } i) .$$

Furthermore, the elasticity tensor reduces to a 3×3 matrix which is denoted by $\tilde{\mathbb{E}}_0$. The same reduction holds true for the deviator operator, given as $\tilde{\mathbb{P}}$. Let us introduce the residual vector for equation (32)₂ in the eigenspace by $\tilde{\mathbf{s}}$. Then, the governing equation for the plastic strains in the eigenspace constitutes as

$$(45) \quad \tilde{\mathbf{s}} := -\tilde{\boldsymbol{\sigma}} + \frac{r^2}{\tilde{\boldsymbol{\sigma}}^{\text{dev}} \cdot \chi^3 \tilde{\mathbb{E}}_0 \cdot \tilde{\boldsymbol{\sigma}}^{\text{dev}}} \tilde{\boldsymbol{\sigma}}^{\text{dev}} \cdot \chi^3 \tilde{\mathbb{E}}_0$$

where we employ also an operator split as $\tilde{\boldsymbol{\sigma}} = \tilde{\boldsymbol{\sigma}}(\boldsymbol{\varepsilon}_{n+1}, \boldsymbol{\varepsilon}_n^p, \chi_n)$. The Newton method for (45) reads

$$(46) \quad \tilde{\mathbf{s}} + \frac{\partial \tilde{\mathbf{s}}}{\partial \tilde{\boldsymbol{\varepsilon}}^p} \cdot \Delta \tilde{\boldsymbol{\varepsilon}}^p = \mathbf{0}$$

and the plastic strains are iteratively updated according to

$$(47) \quad \tilde{\boldsymbol{\varepsilon}}_{n+1}^p \leftarrow \tilde{\boldsymbol{\varepsilon}}_{n+1}^p - \left[\frac{\partial \tilde{\mathbf{s}}}{\partial \tilde{\boldsymbol{\varepsilon}}^p} \right]^{-1} \cdot \tilde{\mathbf{s}} .$$

The initial value for the plastic strains is chosen as $\tilde{\boldsymbol{\varepsilon}}_{n+1}^p = \tilde{\boldsymbol{\varepsilon}}_n^p$. The tangent reads

$$(48) \quad \begin{aligned} \frac{\partial \tilde{\mathbf{s}}}{\partial \tilde{\boldsymbol{\varepsilon}}^p} &= \chi^3 \tilde{\mathbb{E}}_0 + \frac{r^2}{(\tilde{\boldsymbol{\sigma}}^{\text{dev}} \cdot \chi^3 \tilde{\mathbb{E}}_0 \cdot \tilde{\boldsymbol{\sigma}}^{\text{dev}})^2} 2 (\tilde{\mathbb{P}} \cdot \chi^3 \tilde{\mathbb{E}}_0 \cdot \chi^3 \tilde{\mathbb{E}}_0 \cdot \tilde{\boldsymbol{\sigma}}^{\text{dev}}) \otimes (\tilde{\boldsymbol{\sigma}}^{\text{dev}} \cdot \chi^3 \tilde{\mathbb{E}}_0) \\ &\quad - \frac{r^2}{\tilde{\boldsymbol{\sigma}}^{\text{dev}} \cdot \chi^3 \tilde{\mathbb{E}}_0 \cdot \tilde{\boldsymbol{\sigma}}^{\text{dev}}} \tilde{\mathbb{P}} \cdot \chi^3 \tilde{\mathbb{E}}_0 \cdot \chi^3 \tilde{\mathbb{E}}_0 \\ &= \chi^3 \tilde{\mathbb{E}}_0 + \chi^3 r^2 \frac{\tilde{\mathbb{P}} \cdot \tilde{\mathbb{E}}_0}{\tilde{\boldsymbol{\sigma}}^{\text{dev}} \cdot \tilde{\mathbb{E}}_0 \cdot \tilde{\boldsymbol{\sigma}}^{\text{dev}}} \cdot \left(2 \frac{(\tilde{\mathbb{E}}_0 \cdot \tilde{\boldsymbol{\sigma}}^{\text{dev}}) \otimes (\tilde{\boldsymbol{\sigma}}^{\text{dev}} \cdot \tilde{\mathbb{E}}_0)}{\tilde{\boldsymbol{\sigma}}^{\text{dev}} \cdot \tilde{\mathbb{E}}_0 \cdot \tilde{\boldsymbol{\sigma}}^{\text{dev}}} - \tilde{\mathbb{E}}_0 \right) . \end{aligned}$$

After convergence of $\tilde{\mathbf{s}} = \mathbf{0}$, the constraint of volume preservation is accounted for by multiplication with $\tilde{\mathbb{P}}$

$$(49) \quad \tilde{\boldsymbol{\varepsilon}}_{n+1}^p \leftarrow \tilde{\mathbb{P}} \cdot \tilde{\boldsymbol{\varepsilon}}_{n+1}^p ,$$

cf. (32)₂, and the transformation from the eigenspace back into the physical space is carried out by means of

$$(50) \quad \boldsymbol{\varepsilon}_{n+1}^p \leftarrow \mathbf{T} \cdot \text{diag}(\tilde{\boldsymbol{\varepsilon}}_{n+1}^p) \cdot \mathbf{T}^T .$$

Alg. 1 is employed if $\Phi(\boldsymbol{\varepsilon}_{n+1}, \boldsymbol{\varepsilon}_n^p, \chi_n) \geq 0$. Otherwise, i. e. $\Phi < 0$, an elastic material behavior is detected and the plastic strain is set to $\boldsymbol{\varepsilon}_{n+1}^p = \mathbf{0}$.

Algorithm 1 Updating plastic strain if $\Phi(\boldsymbol{\varepsilon}_{n+1}, \boldsymbol{\varepsilon}_n^p, \chi_n) \geq 0$

```

initialize  $\boldsymbol{\varepsilon}_{n+1}^p = \boldsymbol{\varepsilon}_n^p$  ▷ initial-value of plastic strain

transform  $\tilde{\boldsymbol{\varepsilon}}_{n+1}^p \leftarrow \tilde{\boldsymbol{\varepsilon}}_i^p = (\mathbf{T}^T \cdot \boldsymbol{\varepsilon}_{n+1}^p \cdot \mathbf{T})_{ii}$ , see (44) ▷ plastic strain in eigenspace

for  $1, \dots, \max$  do ▷ repeat maximal times

    compute  $\tilde{\mathbf{s}}(\tilde{\boldsymbol{\varepsilon}}_{n+1}^p)$ , see (45) ▷ compute residual vector

    if  $\tilde{\mathbf{s}}(\tilde{\boldsymbol{\varepsilon}}_{n+1}^p) = \mathbf{0}$  then ▷ check convergence of residual vector
        break
    end if

    compute  $\frac{\partial \tilde{\mathbf{s}}}{\partial \tilde{\boldsymbol{\varepsilon}}^p}$ , see (48) ▷ analytical computed tangent

    update  $\tilde{\boldsymbol{\varepsilon}}_{n+1}^p \leftarrow \tilde{\boldsymbol{\varepsilon}}_{n+1}^p - \left[ \frac{\partial \tilde{\mathbf{s}}}{\partial \tilde{\boldsymbol{\varepsilon}}^p} \right]^{-1} \cdot \tilde{\mathbf{s}}$ , see (47) ▷ next plastic strains

end for

compute  $\tilde{\boldsymbol{\varepsilon}}_{n+1}^p \leftarrow \tilde{\mathbb{P}} \cdot \tilde{\boldsymbol{\varepsilon}}_{n+1}^p$ , see (49) ▷ apply volume preservation constraint

back transformation  $\boldsymbol{\varepsilon}_{n+1}^p \leftarrow \mathbf{T} \cdot \text{diag}(\tilde{\boldsymbol{\varepsilon}}_{n+1}^p) \cdot \mathbf{T}^T$ , see (50) ▷ new plastic strain  
in physical space

```

3.3 The update of the density variable

The evolution of the density variable is described by the transient partial differential equation in (32)₃ which needs to be discretized both in time and space for numerical evaluation. Various strategies can be used for this purpose, e.g., a finite element approach would be possible. However, due to constraint of bounded interval for χ and prescribed design volume, a direct FE approach consumes a remarkable amount of computation time, cf. [22], where such a procedure has been discussed. A more advantageous numerical treatment for this equation has therefore been presented in [17] which is based on a generalized finite difference scheme along with an operator split. This procedure has been referred to as Neighbored Element Method (NEM). More details on the numerical performance of the NEM, also regarding important aspects like convergence behavior and robustness, have been investigated in [36]. In this paper, we make use of the published strategies and therefore only recall the fundamental update equation and refer to the original publications for a detailed explanation.

Each value of the topology density field is evaluated for one discrete subvolume. Here, a subvolume is defined as one finite element. The transient character of the evolution equation demands the definition of the initial value for the density variable for each element. As naive guess, we set each discretized density variable to $\chi^{\text{ini}} = \varrho_0$. Therefore, the constraint of the given prescribed structure volume is identically fulfilled.

The transient partial differential equation (32)₃ will be solved in two steps: first, it is nor-

malized with the weighted driving force

$$(51) \quad p_w := \frac{\sum_e (\chi_e - \chi_{\min}) (1 - \chi_e) p_e}{\sum_e (\chi_e - \chi_{\min}) (1 - \chi_e)},$$

see equation (36) in [17]. Accounting for the normalization, we define $\bar{p} := p/p_w$, $\eta^* := \eta/p_w$, $\beta^* := \beta/p_w$, $\lambda_\chi^* := \lambda_\chi/p_w$, and $\gamma^* := \gamma/p_w$. Subsequently, the update scheme according to NEM is employed, cf. [17]. Then, the discretized evolution equation for the density variable for each element is given by

$$(52) \quad \chi_{n+1} = \chi_n + \Delta t \frac{1}{\eta^*} [-\bar{p}_{n+1} + \beta^* \Delta \chi_n + \lambda_\chi^* + \gamma^*]$$

analogously to equation (49) in [21]. Due to this, we are able to account for the regularization parameter β^* in length unit squared and the viscosity η^* in time unit as general optimization parameters.

To determine the value of the Lagrange parameter λ_χ^* for the volume constraint, the update equation (52) is solved iteratively by a simple bisection algorithm analogously to Alg. 1 in [17]. This process also determindes γ^* .

In case that this update schemes shows numerical instabilities, a more advanced update scheme has been presented in [17] which can also applied to thermodynamic topology including plasticity. However, for all numerical examples considered here, no further numerical stabilization was necessary.

3.4 Optimization process

The presented update schemes take place in a global optimization process. First the update of the displacements \mathbf{u}_{n+1} is solved by the finite element method for fixated values of the plastic strains at the previous global iteration step $\boldsymbol{\varepsilon}_n^p$. After updating the displacements, both the update of the plastic strains $\boldsymbol{\varepsilon}_{n+1}^p$ and the update of the density variable χ_{n+1} are performed using the updated displacements \mathbf{u}_{n+1} . The updated value for the plastic strains and the density variable are used for updating the displacements in the succeeding global iteration step $n \leftarrow n + 1$.

The entire flowchart of the thermodynamic topology optimization including plasticity is given in Fig. 7.

4 Numerical results

We present several aspects of our novel thermodynamic topology optimization including plasticity by investigation of various numerical experiments. We begin with the presentation of the general functionality of the proposed surrogate material model for plasticity on the material point level. Afterwards, we show the impact of the material model on the optimized construction parts by means of analyzing several quasi 2D and 3D boundary value problems. All results are based on the numerical implementation with Julia programming language [2]. If not stated differently, we use the material parameter for steel summarized in Tab. 1.

All simulations resulting from the optimization are based on hexahedral finite element meshes with linear shape functions. The illustrations of the field data are created with Paraview [3]. The resultant structures are obtained by using the isovolume filter for the density variable χ with the minimum threshold set to 0.5. This is the average value of the interval in which χ has been defined. When available, our results will be verified by comparison to previous research findings.

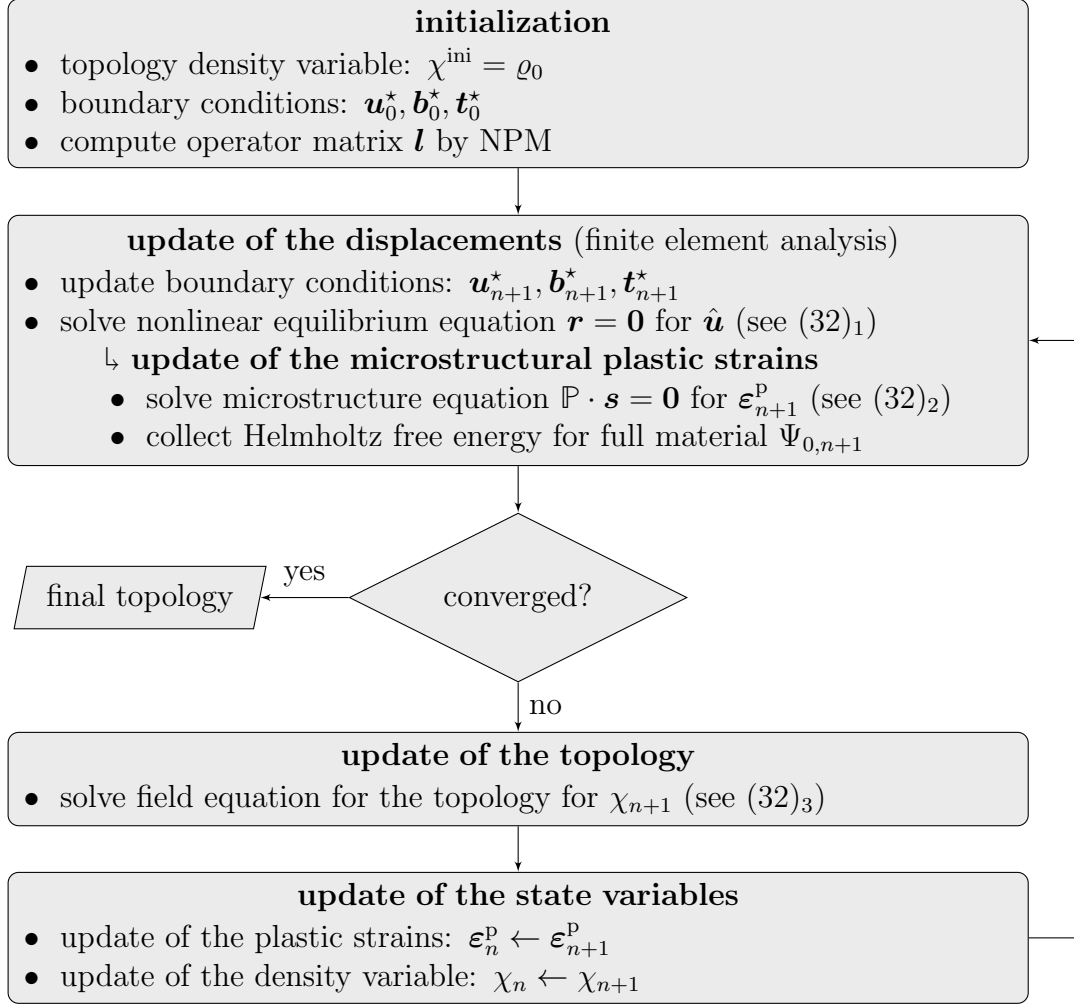


Figure 7: Flowchart of the numerical implementation of the thermodynamic topology optimization including plasticity

Table 1: Material parameters

	Young's module E_0 [MPa]	Poisson's ratio ν [-]	yield stress $\sigma_{\text{exp}}^{\text{Y}}$ [MPa]
steel	210 000	0.3	300

4.1 Material model

The computation of plastic strain takes place at the microstructural level. To investigate the results of the proposed surrogate material model for plasticity without dissipation, we present a first result at the material point and thus without topology optimization. Consequently, we prescribe the strain as linear function of the load steps according to Fig. 8. The loading path includes both loading and unloading. The material model is tested for the prescribed strain according to

$$(53) \quad \boldsymbol{\varepsilon}(l) = \varepsilon_{11}(l) \begin{pmatrix} 1 & 0.7 & 0.7 \\ 0.7 & -\nu & -0.1 \\ 0.7 & -0.1 & -\nu \end{pmatrix}.$$

To present a result that is representative, we have chosen the diagonal entries to correspond to the material parameters given above, i. e., we use the Poisson's ratio of steel; the amplitudes of the shear components have been chosen randomly.

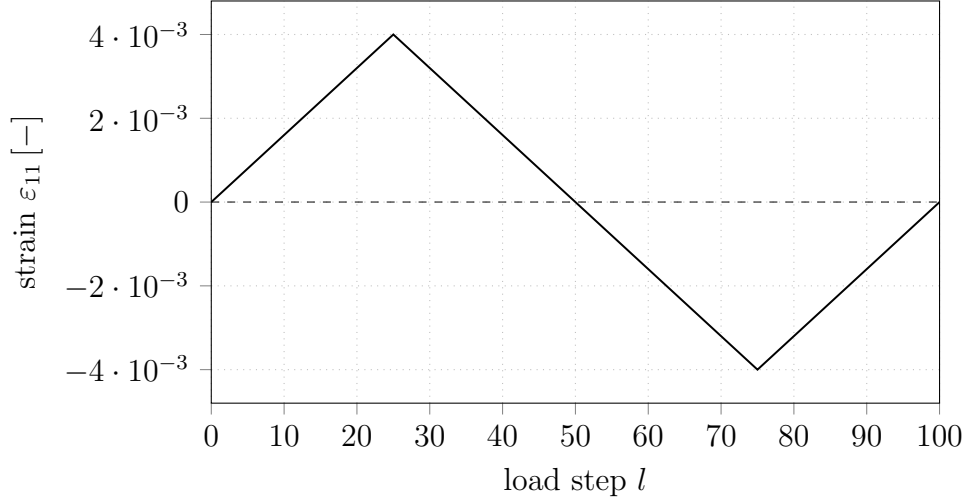


Figure 8: Prescribed strain at the material point level as function of the load steps l

The numerical results for the prescribed strain for loading and unloading at the material point level is given in Fig. 9 as stress/strain diagram. It indicates that the intended material behavior is displayed: first, the stress/strain curve of the proposed material model increases linearly in the elastic region. The end points of the elastic region are indicated by $\varepsilon_{\text{exp}}^Y$ and σ_{exp}^Y , respectively. The shift between the regions is influenced by the number of the chosen step size. Then, the stress reaches the yield stress level in the plastic case. This behavior coincides to classical plasticity models. However, the remarkable difference is that the unloading case is also included in Fig. 9. Here, no hysteresis is observed which is intended to always display a stress

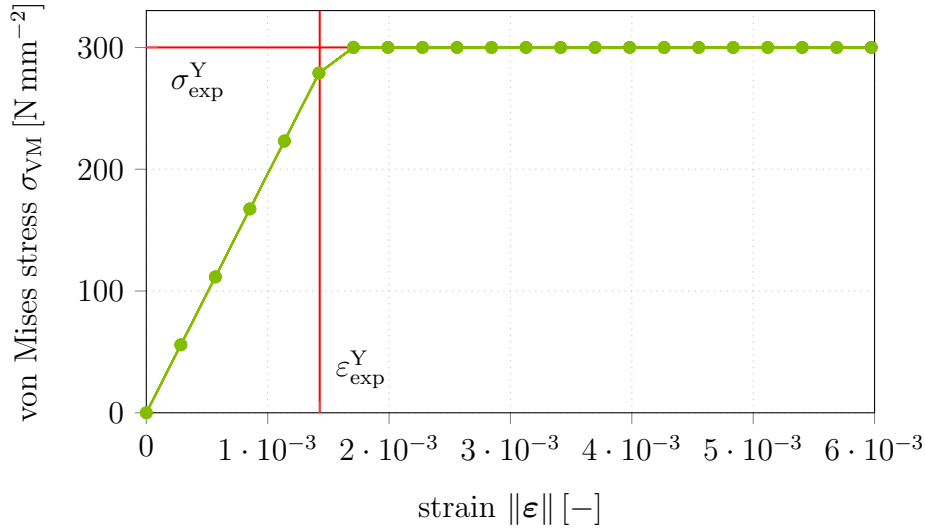


Figure 9: Stress/strain diagram for the dissipation-free plasticity model

state which would results for a pure physical loading and is not effected by virtual unloading due to the optimization process. The result is thus independent of the unloading history.

Moreover, we compare the surrogate material model and the hysteresis curve for a classical elasto-plastic model accounting for one component of the stress/strain state. Thus, both curves are shown in Fig. 10a. The behavior for loading and unloading can be observed in greater detail by considering the corresponding stress deviator and plastic strain vs the load steps in Fig. 10b and Fig. 10c, respectively, for both material models. Here, it becomes obvious that the stress in the surrogate material model decreases linearly but only after reaching the critical

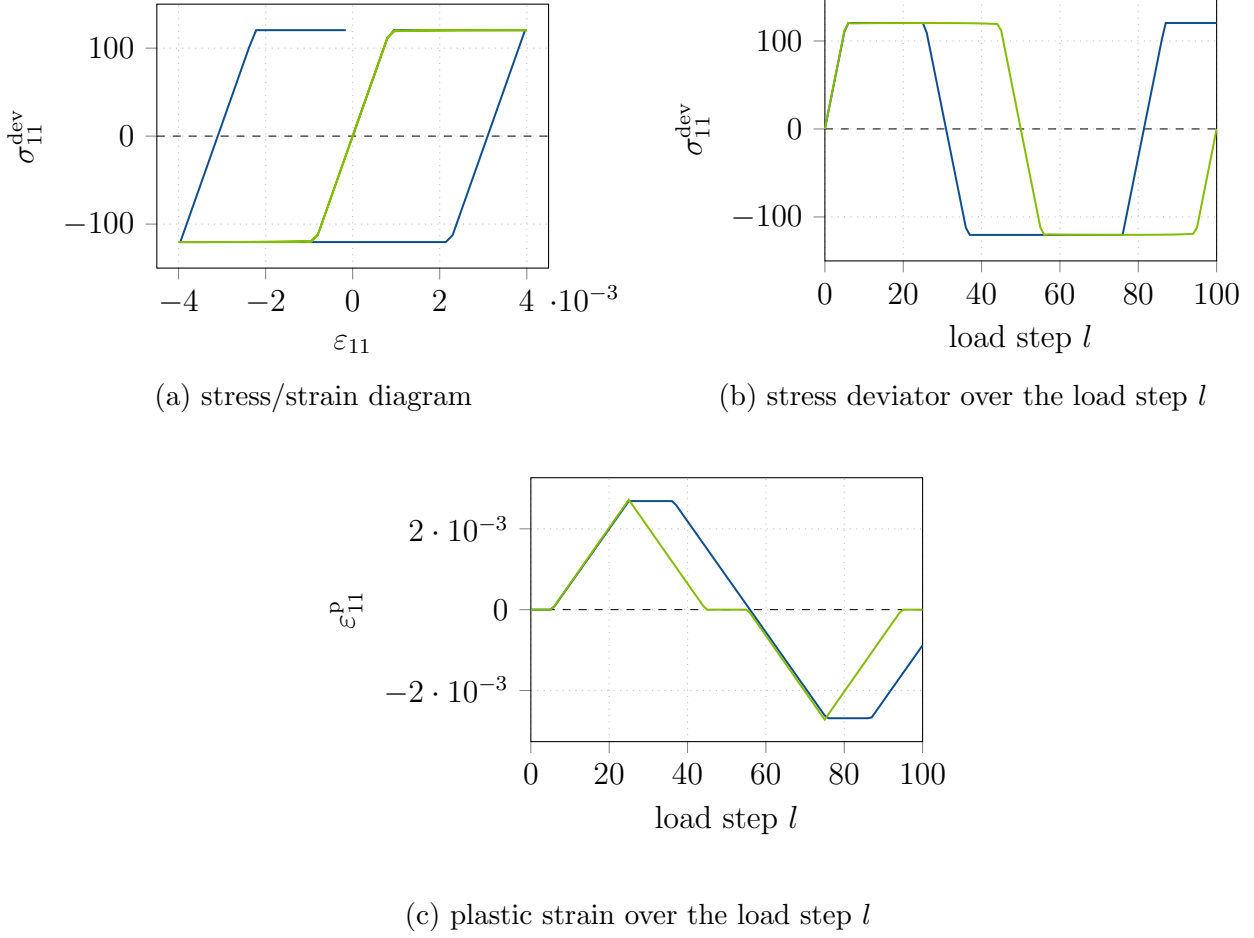


Figure 10: Comparison of the stress behavior of classical elasto-plastic (blue) and surrogate material model (green)

elastic strain ϵ_{exp}^Y . Correspondingly, the increase or decrease of plastic strains in the surrogate material model directly reacts on the increase or decrease of strains in the plastic case. As a result, the surrogate material model deviates from the purely physical classical elasto-plastic material behavior exactly as intended. This indeed allows to compute all stress states only from loading conditions, even if the local strains are reduced due to the evolving topology and thus increasing stiffness. The same behavior would result for classical material models if they are always evaluated starting from a virgin microstructure, i. e. initially using $\epsilon^p = \mathbf{0}$ to compute the stress state for all load steps. Furthermore, it is worth mentioning that we obtain exactly the behavior as for hyperelastic surrogate model in the 1D case. However, our surrogate material model yields the intended results also for the 3D case in which the calibration of an hyperelastic model is a very challenging task, if possible at all.

In order to verify the surrogate material model in 3D, let us investigate individual components of the deviatoric stress which are given in Fig. 11. The individual components of the stress deviator have, of course, different stress levels in the plastic regime which are determined by the specific strain state in (53). The resulting norm (cf. Fig. 9) corresponds to the given yield criterion.

We have therefore numerically shown that the developed surrogate material model fulfills the intended purpose of displaying a physically plastic material behavior but without considering dissipation.

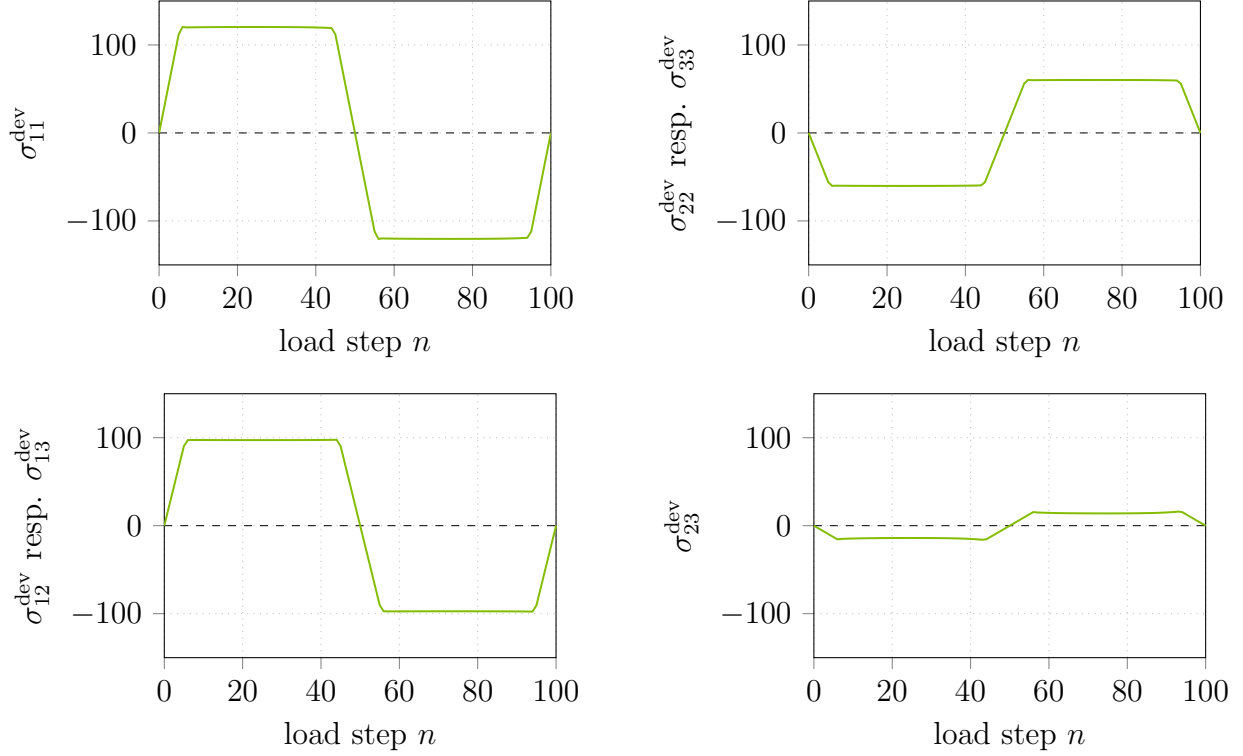


Figure 11: Evolution of the components of stress deviator over the load steps l

4.2 Optimization results

4.2.1 Benchmark problems

To demonstrate the functionality of the consideration of plasticity in the thermodynamic topology optimization, several boundary value problems are tested. To this end, we present all considered design spaces with the respective boundary conditions. Here, the thickness of the quasi 2D models is discretized by one finite element. The surrogate model for plasticity results in a non-linear stress/strain relation. Consequently, to analyze the behavior of the optimization for the non-linear material model, the load conditions are applied as prescribed displacements. Additionally, the specifics of force-controlled optimizations are presented in Sec. 4.2.4.

The first boundary problem is the quasi 2D classical Messerschmitt-Bölkow-Blohm (MBB) beam shown in Fig. 12. It is simply supported at the lower corner nodes and it is loaded centrally from above. Furthermore, a cantilever in quasi 2D is investigated. The rectangular geometry is

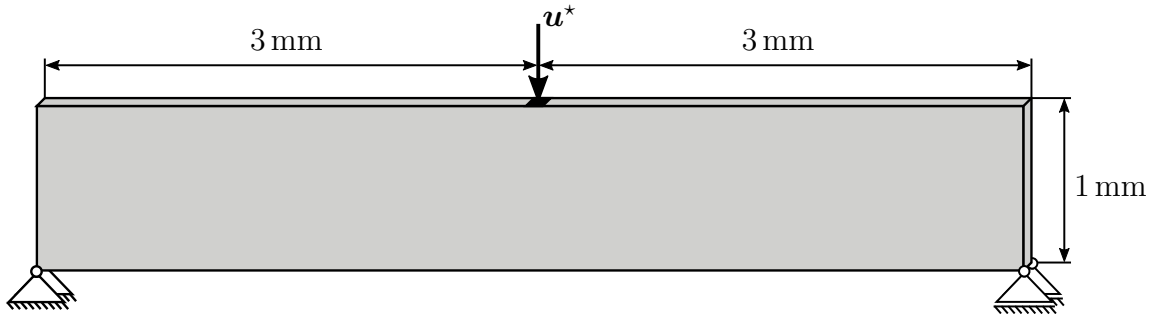


Figure 12: Dimensions and boundary conditions for the quasi 2D MBB beam

shown in Fig. 13: it is supported at the left-hand side and loaded at the right-hand side. As an

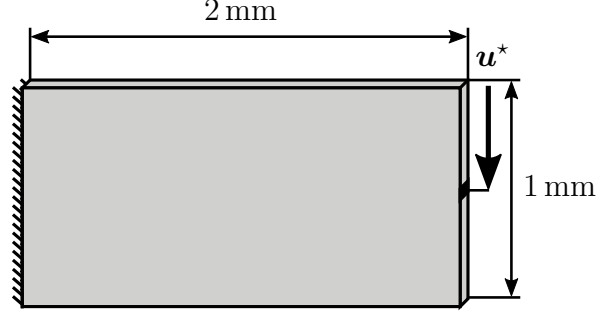


Figure 13: Dimensions and boundary conditions for the quasi 2D cantilever

example including a singularity due to the geometry of the design space, we also consider a quasi 2D L-shaped cantilever which is loaded as indicated in Fig. 14. The clamped beam in Fig. 15 is

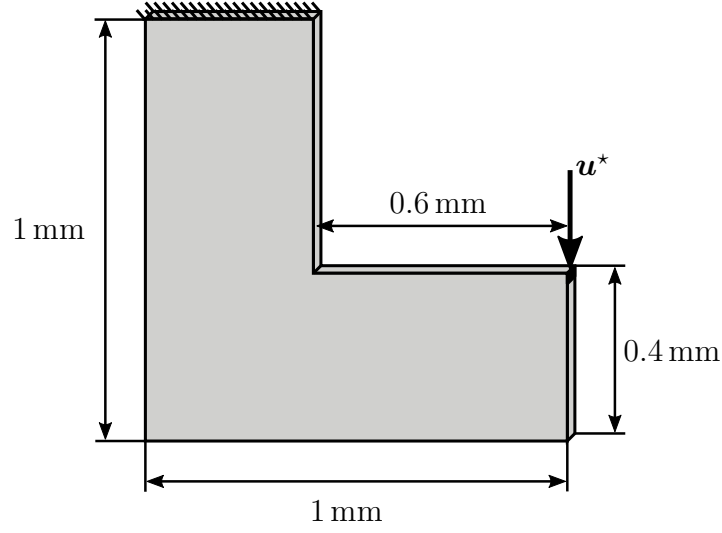


Figure 14: Dimensions and boundary conditions for the quasi 2D L-shaped cantilever

fixated at both sides and chosen in analogy to Maute *et al.* [26]. As 3D example, we investigate

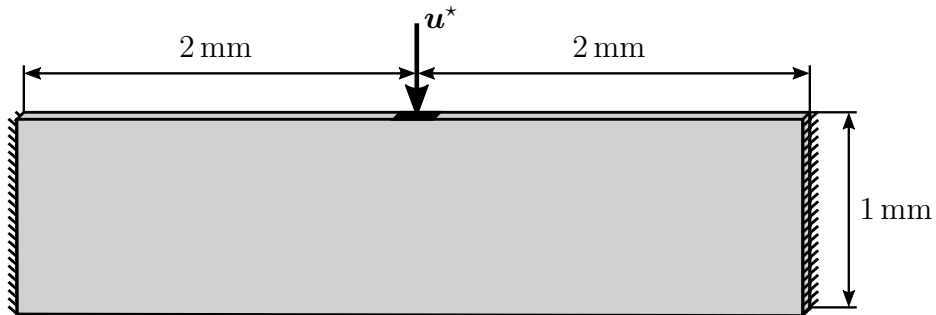


Figure 15: Dimensions and boundary conditions for the quasi 2D clamped beam

the boundary value problem given in Fig. 16. The four corners of one side are fixated and the force is exerted at the bottom of the opposite side.

All necessary model and material parameters for the different boundary value problems are collected in Tab. 2.

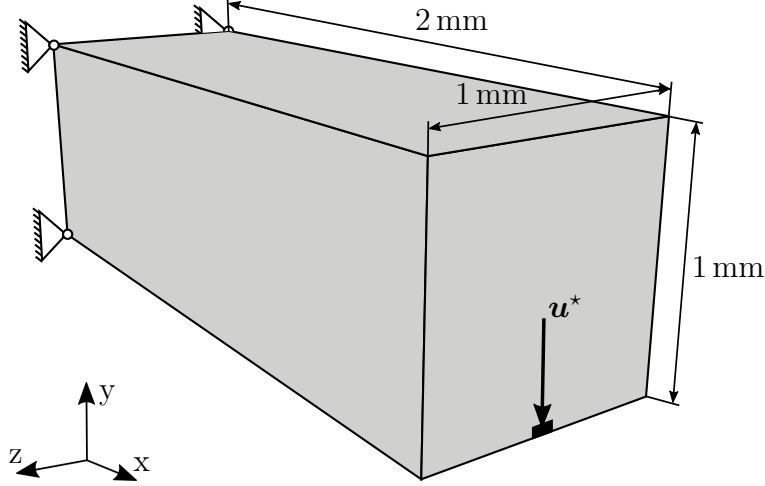


Figure 16: Dimensions and boundary conditions for the 3D cantilever

Table 2: Model parameters

boundary value problem	#elements	u^* [mm]	ϱ_0 [–]	η^* [s]	β^* [mm ²]
quasi 2D MBB beam	2400	0.020	0.50	15	5.00×10^{-3}
	9600	0.020	0.50	15	1.25×10^{-3}
quasi 2D cantilever	3200	0.010	0.50	15	1.25×10^{-3}
	12 800	0.010	0.50	15	0.31×10^{-3}
quasi 2D L-shaped cantilever	4032	0.007	0.50	15	0.31×10^{-3}
quasi 2D clamped beam	10 000	0.030	0.32	15	0.80×10^{-3}
3D cantilever	41 472	0.060	0.18	15	5.21×10^{-3}

It is worth mentioning that in contrast to topology optimization of linear elastic materials, our results depend in a non-linear way on the amplitude of load (which might be provided either by external forces or prescribed displacements).

It is furthermore worth mentioning that maximum loading, i. e., the loading for which the structure is optimized, can be employed instantaneously: we obtained identical structures no matter whether the load was applied within one single or several load steps. This is a remarkable difference to other optimization schemes including plasticity. Our novel surrogate model allows to account for a physically reasonable computation of the plastic strains without repeating the entire loading history for each optimization step which is usually necessary to estimate the sensitivity. Since the solution of the finite element problem consumes the highest amount of computation time, our novel approach enables us to save numerical costs in the order of magnitudes.

The minimum value for the density variable is set to $\chi_{\min} = 0.001$ such that the minimal stiffness is given by $10^{-9} \times \mathbb{E}_0$. Depending on the discretization, i. e., the maximum finite element size which is indicated by h_{\max} , the regularization parameter is chosen as $\beta^* = 2 h_{\max}^2 \text{mm}^2$ if not stated differently. To avoid interrupted truss elements at the 3D cantilever, it can be necessary to choose a slightly bigger value, i. e., $\beta^* = 3 h_{\max}^2 \text{mm}^2$, for instance. Then, based on our previous work [17], the smallest structure dimensions can be realized by the optimization scheme without showing the checkerboard phenomenon and thus yielding mesh-dependent finite element results (for values with $\beta^* < 2 h_{\max}^2$, no sufficient regularization is employed which turns the optimization problem to be mathematically ill-posed). Moreover, β^* controls the member size by the minimum structure radius $R_{\min} \approx \sqrt{\beta^*}$. Both can be seen in Fig. 17, where the same β^* is used for different mesh discretizations and the optimization results show the same,

mesh-independent structures.



Figure 17: Comparative results with $\beta^* = 1.25 \times 10^{-3} \text{ mm}^2$ for a coarse ($\#_{\text{elements}} = 3200$) and a fine ($\#_{\text{elements}} = 12\,800$) meshed quasi 2D cantilever in a force-controlled optimization

The viscosity for all simulations is set to $\eta^* = 15 \text{ s}$. Using smaller values for the viscosity results in a faster evolution of the topology at the expense of a reduced numerical stability. On the other hand, larger values increase the stability at the expense of a remarkably increased total computation time: here, a remarkably higher number of finite element iterations is necessary which is the bottleneck of the computational costs. Consequently, large values for η^* should be avoided. In case of using small values for the viscosity, the numerical scheme in [17] provides a possible solution.

4.2.2 Structure analysis

As first aspect, we investigate the impact of inclusion of plasticity on the resultant optimal structure. To this end, the optimization results are compared with results of thermodynamic topology optimization for a linear elastic material behavior. This can be achieved while setting the yield stress to an unphysically high value, i.e. $\sigma_{\text{exp}}^Y = 100\,000 \text{ MPa}$. This ensures that no plastic deformation is active since the von Mises norm of the stress is below this value for all boundary value problems considered. The results obtained from this elastic optimizations are consistent with results obtained in our previous publications, cf. [17], for instance. All structures are presented for the last iteration step.

For all results, the green structure corresponds to the thermodynamic topology optimization including plasticity whereas the gray structure is the result for a purely linear elastic topology optimization. If possible, symmetry planes are used to simplify the comparison between plastic and elastic structures. For some boundary value problems, we also compute structures with varying minimum member size by increase the number of finite elements and consequently reducing the regularization parameter β^* . However, finer structures only evolve if beneficial for the increase of total stiffness. For instance, we did not observe finer structures for the L-shaped cantilever when a finer finite element mesh is used. Therefore, we dispense to present this result.

As general conclusion, we observe that the structures including plasticity contain slightly thicker but shorter truss elements. The effect of this is obvious: thicker cross section areas reduce the maximum value of the averaged stress such that the remaining stress is limited by the yield stress. Furthermore, the onset of plasticity includes remarkable reduction of stiffness since locally higher strains do not result in higher stress: the yield stress is the upper limit. This physically reasonable behavior results in a “deactivation” of material points, which undergo yielding, for the contribution to the global stiffness of the structure. Consequently, remarkably difference structures are computed when plastic material behavior is considered.

The components of the structures, at which the highest stresses and thus plastic deformations are present, are found at the constrained boundaries in terms of external loading and supports.

Consequently, we observe thicker member sizes here, cf. the center of the MBB beam with acting force in Fig. 18 and the supports for the quasi 2D cantilever in Fig. 19. For the MBB beam

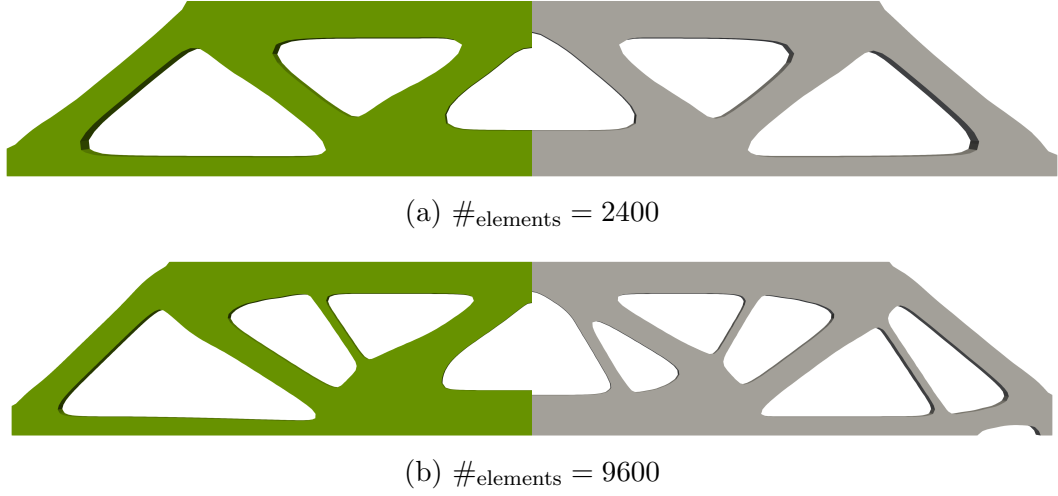


Figure 18: Comparative results for plastic (green) and elastic (gray) displacement-controlled optimization for the quasi 2D MBB beam



Figure 19: Comparative results for plastic (green) and elastic (gray) displacement-controlled optimization for the quasi 2D cantilever

and the cantilever, a difference can be detected between the coarse and fine mesh. Especially, for the finer mesh, different truss elements evolves in comparison to the elastic structures. This was also noted by Duysinx and Bendsøe [12] who account for a local stress criteria. There, results for force-controlled optimization basically fits the arrangement of truss elements as mentioned here. More significant differences are detected in comparison with the results by Zhao *et al.* [41], who consider a non-linear hyperelastic surrogate model accounting for the Drucker-Prager criterion.

The modification of the thickness of the trusses, of course, also has an impact on the total structure regarding the general topology: due to prescribed total structure volume, the angles and thicknesses of some bars change significantly for the plastic optimization. A remarkable increase of “thickness” is observed in the corner of the L-shaped cantilever in Fig. 20 which was anticipated due to the stress singularity. This popular example is also taken into account by mentioned approaches considering local [10, 24] or global [6] stress constraints. The difference between the elastic and the plastic optimized structure can be detected as an additional truss element at the bottom left side. This design with the additional truss for the critical notch was also detected in [10, 6].

A particularly example for a remarkably different structure due to topology optimization accounting for plasticity can be seen for the two side clamped beam in Fig. 21. Due to plasticity, significantly different truss forms are established which allow the stresses to follow a more



Figure 20: Comparative results for plastic (green) and elastic (gray) displacement-controlled optimization for the quasi 2D L-shaped cantilever



Figure 21: Comparative results for plastic (green) and elastic (gray) displacement-controlled optimization for the quasi 2D clamped beam

favorable load path. This finding also corresponds to the results by Maute *et al.* [26] who make use of a classical elasto-plastic material model including the additional finite element simulations for plasticity as discussed. Zhao *et al.* [42] especially focus on this example and they are able to achieve a similar structure with their non-linear elastic surrogate model. Also, the structure resulting of the topology optimization accounting for finite strain plasticity by Wallin *et al.* [37] has similar characteristics.

The optimization results of the 3D cantilever seen in Fig. 22 proves the functionality and applicability of our approach for fully 3D boundary problems.

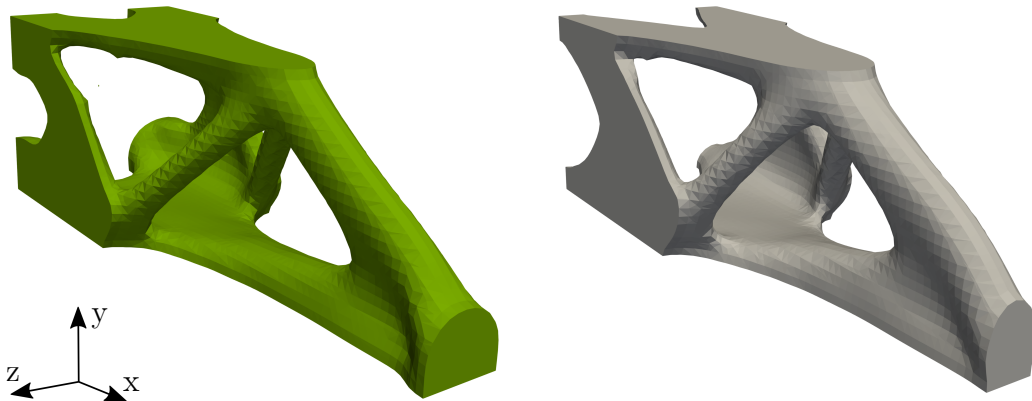


Figure 22: Comparative results for plastic (green) and elastic (gray) displacements-controlled optimization for the 3D cantilever

4.2.3 Convergence behavior

Another aspect of the analysis is to discuss the evolution of the optimization objective which is to minimize the compliance of the structure. Since a compliance minimization analogously causes a stiffness maximization, we use the latter for presentation. The stiffness is computed in analogy to other works on topology optimization by $1/\mathbf{f} \cdot \hat{\mathbf{u}}$ and scaled by the initial stiffness (cf. Tab. 3) of the homogeneously gray density distribution for each boundary value problem.

Table 3: Overview of the initial stiffness values S_0 for the homogeneously gray density distribution

boundary value problem	#elements	abs. S_0 [$\text{N}^{-1} \text{mm}^{-1}$]
quasi 2D MBB beam	2400	27.202×10^{-3}
	9600	7.091×10^{-3}
quasi 2D cantilever	3200	18.513×10^{-3}
	12 800	4.647×10^{-3}
quasi 2D L-shaped cantilever	4032	30.003×10^{-3}
quasi 2D clamped beam	10 000	0.961×10^{-3}
3D cantilever	41 472	10.148×10^{-3}

Consequently, we expect a decreasing function for $1/\mathbf{f} \cdot \hat{\mathbf{u}}^*$ when the reaction force increases during the evolution of the structure. The stiffness is plotted as function of the iteration steps for each boundary value problem described above. For all boundary value problems, we define convergence as soon as the relative stiffness changes by less than 1×10^{-4} for 3 succeeding iteration steps. This rather strict convergence criterion is chosen to exclude a wrong detection of convergence in the plastic case.

Due to the explicit discretization of the finite element method, no more than two Newton iterations are in general necessary for convergence of the displacement field. Additionally, due to the operator split, only one optimization step including plasticity is needed.

As general observation, we can conclude that the stiffness of structures including plasticity is lower than of those which behave purely elastically, cf. Fig. 23 for the MBB beam, Fig. 24 for the L-shaped cantilever, Fig. 25 for the clamped beam and Fig. 26 for the 3D cantilever. This

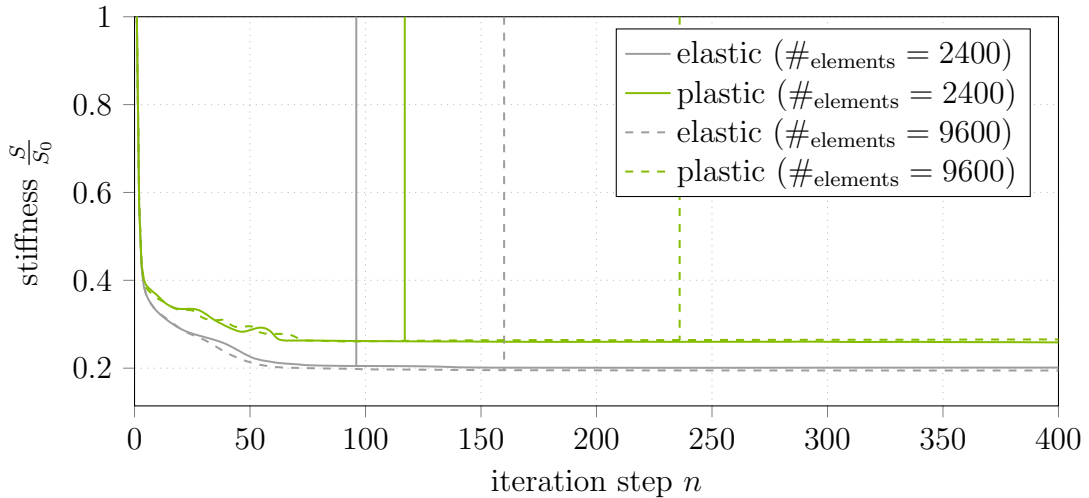


Figure 23: Evolution of stiffness for the displacement-controlled quasi 2D MBB beam. The first time that the convergence criterion has been reach is indicated by a vertical line

is an obvious result: plastic deformations result a yielding of the material such that locally the

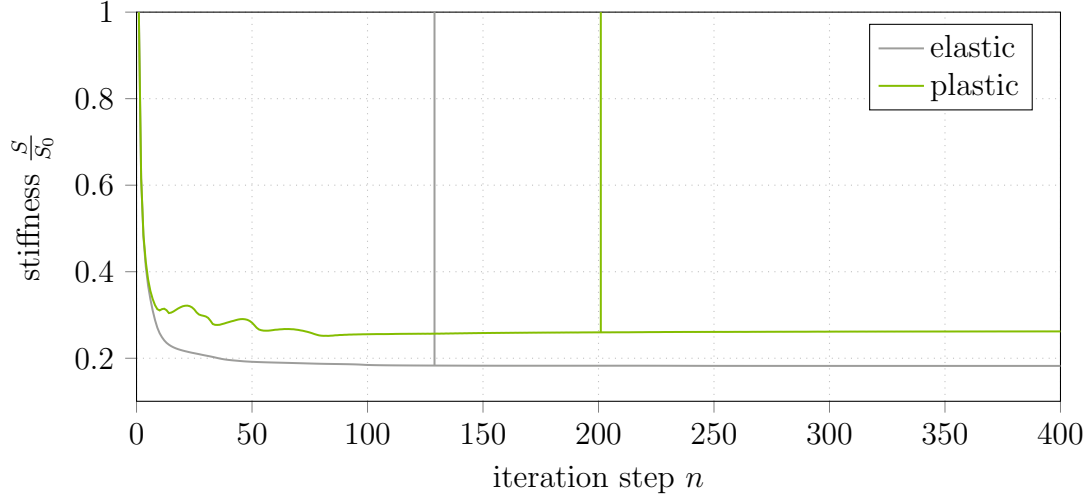


Figure 24: Evolution of stiffness for the displacement-controlled L-shaped cantilever. The first time that the convergence criterion has been reach is indicated by a vertical line

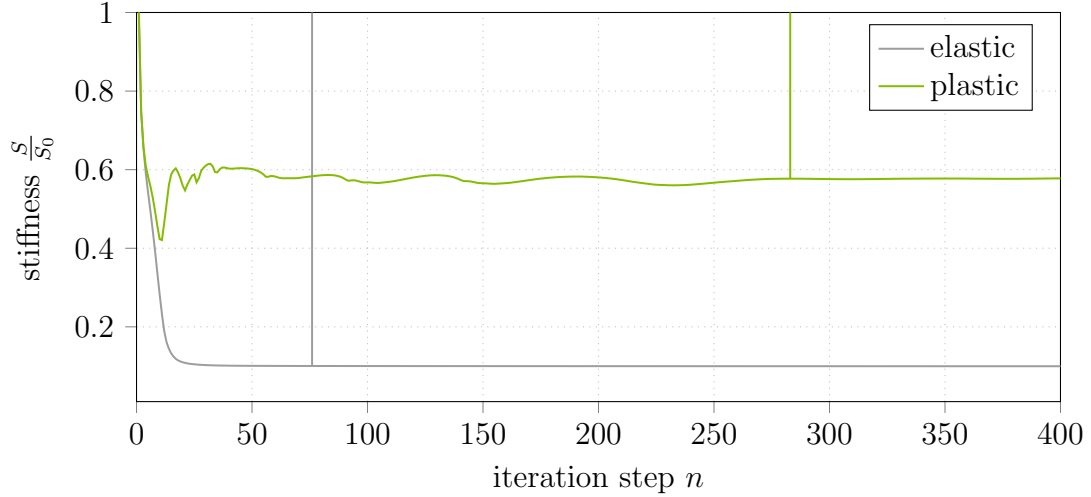


Figure 25: Evolution of stiffness for the displacement-controlled quasi 2D clamped beam. The first time that the convergence criterion has been reach is indicated by a vertical line

stiffness is remarkably reduced which, of course, also reduces the global stiffness. In general, the (absolute value of the) differences in the stiffness plots corresponds to the dissipated energy due to plastic deformations. However, we still see the usual evolution of the stiffness during topology optimization which is that the stiffness increases while a discrete black/white structure evolves. In the elastic case, the maximum stiffness converges towards a constant value.

However, one interesting behavior is given in Fig. 27 for the fine discretization of the quasi 2D cantilever: here, the fraction S/S_0 continues to increase again after reaching some minimal value at $n = 75$. The reason for the increasing function is the reduction of the reaction force in the course of the evolution. This at first glance surprising result is caused by a continued evolution of structure which is driven by the imbalance of local source terms and the Laplace term. Since we do not explicitly account for the optimization of S , a larger priority is set to solve in field equation for χ during the numerical treatment. This evolution process if continued even at the expense of a reduction of stiffness as present for this boundary value problem and the chosen material and model parameters.

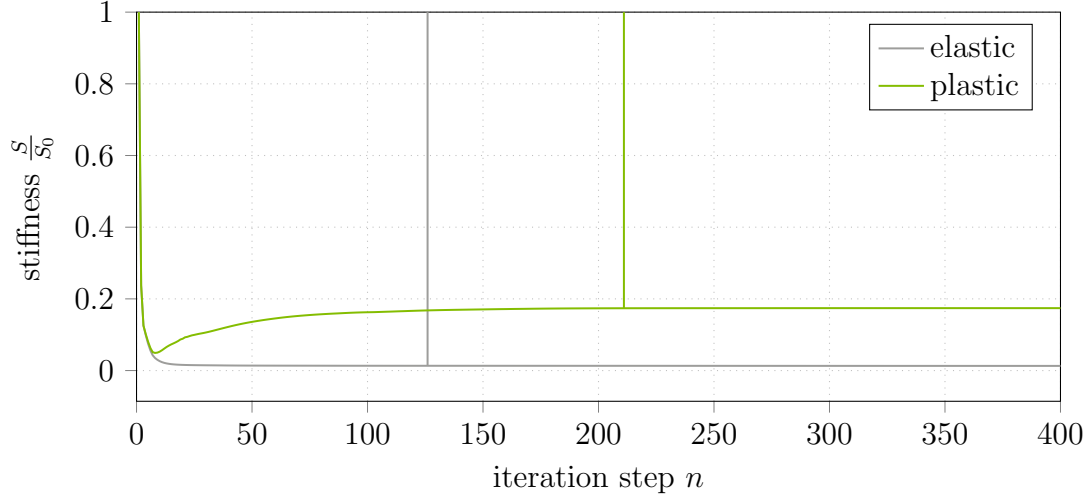


Figure 26: Evolution of stiffness for the displacement-controlled 3D cantilever. The first time that the convergence criterion has been reach is indicated by a vertical line

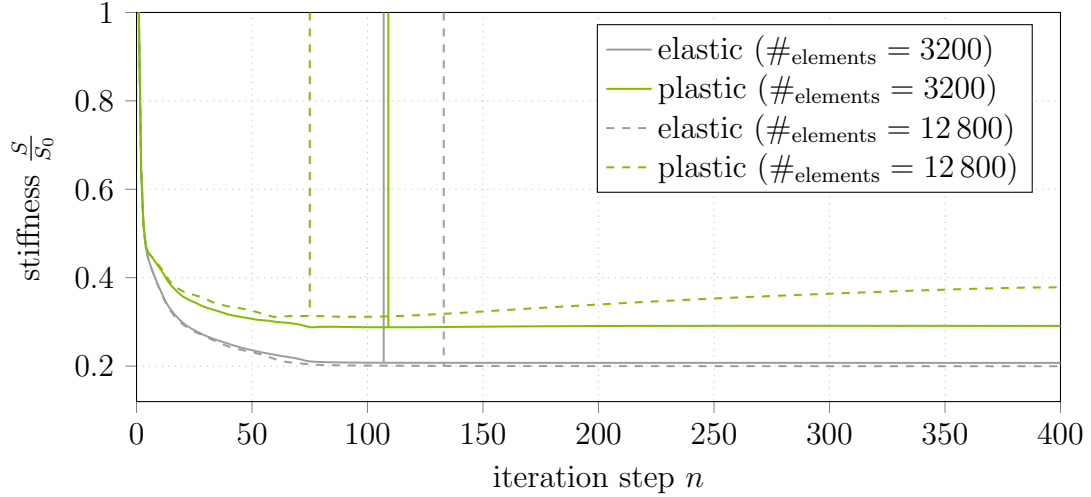


Figure 27: Evolution of stiffness for the displacement-controlled quasi 2D cantilever. The first time that the convergence criterion has been reach is indicated by a vertical line

4.2.4 Force-controlled optimizations

Due to the non-linearity of the surrogate material model, the topology of the optimized structures depends on whether the load is given in terms of prescribed forces or prescribed displacements: during a force-controlled optimization, the initially gray density distribution corresponds to a very small stiffness such that severe deformations are present. Over the course of density evolution, the stiffness increases and the displacements become smaller and smaller. The opposite is true for deformation-controlled simulations: here, the maximum deformation is set and during the structure evolution the resultant forces become larger and larger due to the increase of stiffness. This remarkably different evolution of the deformation state is the reason for different optimal structures for the force- and the displacement-controlled case and routes back to the evolutionary character of our optimization approach. For instance, this can result in minor variations of the bar positions in the L-shaped cantilever, cf. Fig. 28 loaded with $\mathbf{f}^* = 0.0975 \text{ N}$ but also a complete rearrangement of bars might be the outcome as seen in Fig. 29 for the fine MBB beam loaded with $\mathbf{f}^* = 0.99 \text{ N}$. Obviously, structures optimized with an elastic material behavior are identical if only the external force or prescribed displacement have the



Figure 28: Comparative results for plastic (green) and elastic (gray) force-controlled optimization for the quasi 2D L-shaped cantilever

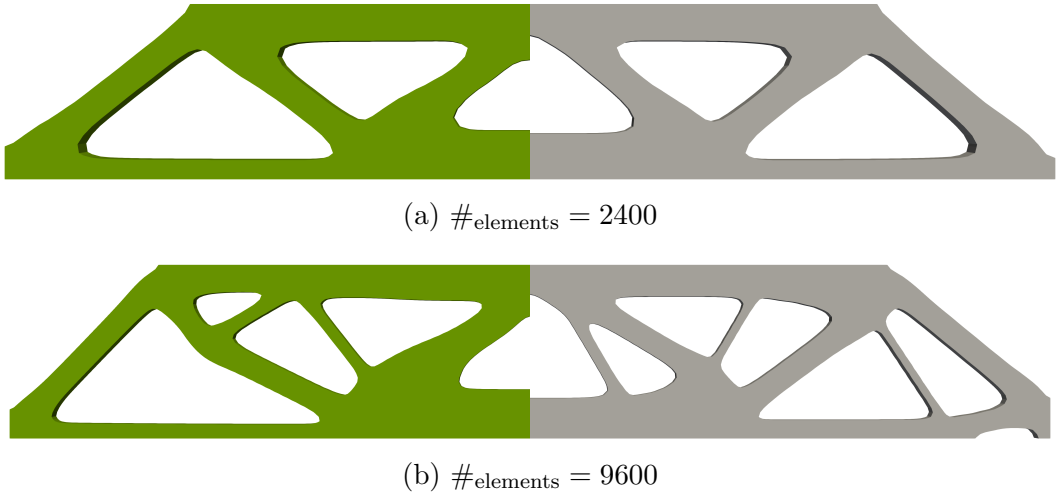


Figure 29: Comparative results for plastic (green) and elastic (gray) force-controlled optimization for the quasi 2D MBB beam

same direction and points of application.

Furthermore, we account for a multi-load case for the quasi 2D L-shaped cantilever. Here, the first load case is defined as a monotonic loading with $\mathbf{f}^* = \mathbf{f}_{\downarrow}^* = 0.0975 \text{ N}$ (analogous to the displacement, cf. Fig. 14). The second load case is defined by a perpendicular tension force $\mathbf{f}_{\rightarrow}^* = 0.0975 \text{ N}$. The support is identical for both load cases as defined before. During the optimization process, the displacement field and consequently the driving forces are computed independently for both load cases. The design update is performed by using the average value of the respective driving forces for both load cases. The optimization result is shown in Fig. 30. The difference to the result for monotonic loading is obvious.

Analyzing the stiffness for a force-controlled optimizations, we have $1/\mathbf{f}^* \cdot \hat{\mathbf{u}}$. Therefore, we may expect an increasing function for the stiffness when the force is prescribed (decreasing nodal displacements during the evolution of structure). In general, the stiffness of force-controlled optimizations corresponds to smaller stiffness values, so that S/S_0 result in larger values. The forces and initial stiffness values S_0 are summarized in Tab. 4.

One example is given for the MBB beam in Fig. 31.

Espacially for force-controlled structures with plastic material behavior, the stiffness may also decrease after reaching some maximum value, cf. Fig. 32 for the fine MBB beam when only the corner nodes of the corner finite elements are supported. This, at first glance, rather surprising behavior can be explained when investigating the deformed configuration of the structure as given

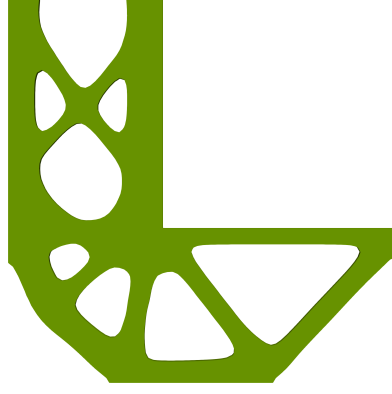


Figure 30: Results for plastic displacement-controlled optimizations with a multi load case for the quasi 2D L-shaped cantilever: load case 1: $\mathbf{f}_{\downarrow}^*$ and load case 2: $\mathbf{f}_{\rightarrow}^*$

Table 4: Overview of the initial stiffness values S_0 for the homogeneously gray density distribution of the selected examples for force-controlled optimizations.

boundary value problem	\mathbf{f}^* [N]	$\#_{\text{elements}}$	abs. S_0 [$\text{N}^{-1} \text{mm}^{-1}$]
quasi 2D MBB beam (one node support)	1.9800	2400	14.623×10^{-4}
	0.9900	9600	3.351×10^{-4}
	0.9900	9600	3.329×10^{-4}
quasi 2D L-shaped cantilever	0.0975	4032	11.250×10^{-4}
quasi 2D L-shaped cantilever	0.1200	4032	7.427×10^{-4}
quasi 2D L-shaped cantilever	0.1500	4032	4.753×10^{-4}

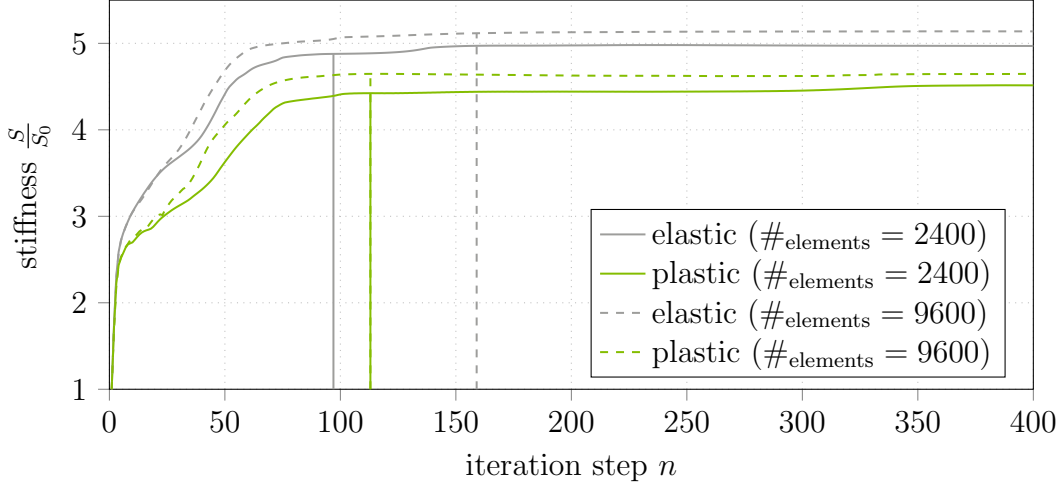


Figure 31: Evolution of stiffness for the force-controlled quasi 2D MBB beam. The first time that the convergence criterion has been reach is indicated by a vertical line

in Fig. 33. Due to the load that exceeds the maximum bearable value, the material fails which manifests in a non-converging deformation at the supports and/or at boundary with prescribed load. Since the stiffness can be computed by $1/\mathbf{f}^* \cdot \hat{\mathbf{u}}$, stiffness may reduce when the deformation continues to increase for a constant load. Therefore, the physical problem just does not provide a solution: the load is too high to cause a microstructural state including plastic deformations that is stable and would be able to carry this load, i. e., the material continues to yield. On the other hand, we observe a smooth convergence also for the plastic optimization for a smaller loading. This general observation also holds true for the other boundary value problems, cf.

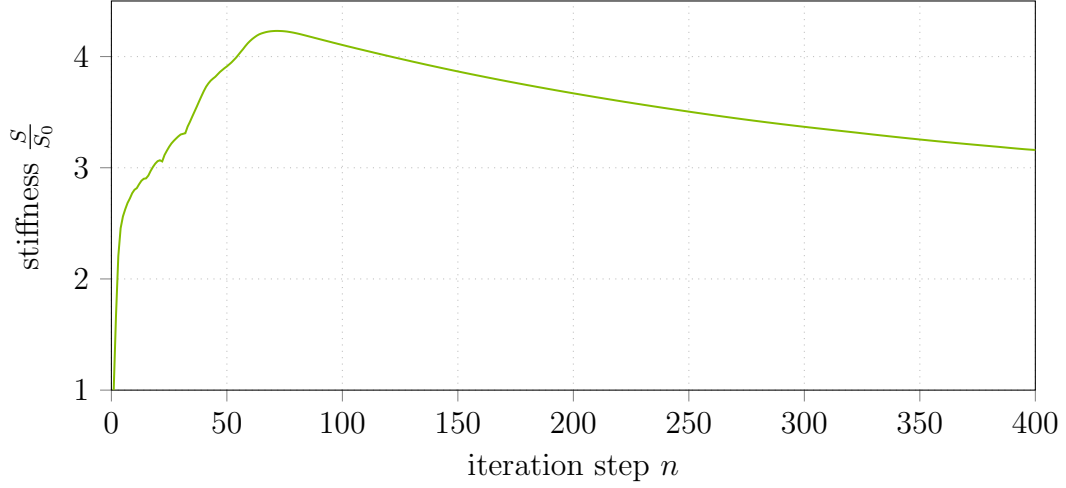


Figure 32: Evolution of stiffness for the force-controlled quasi 2D MBB beam when only the corner nodes are supported

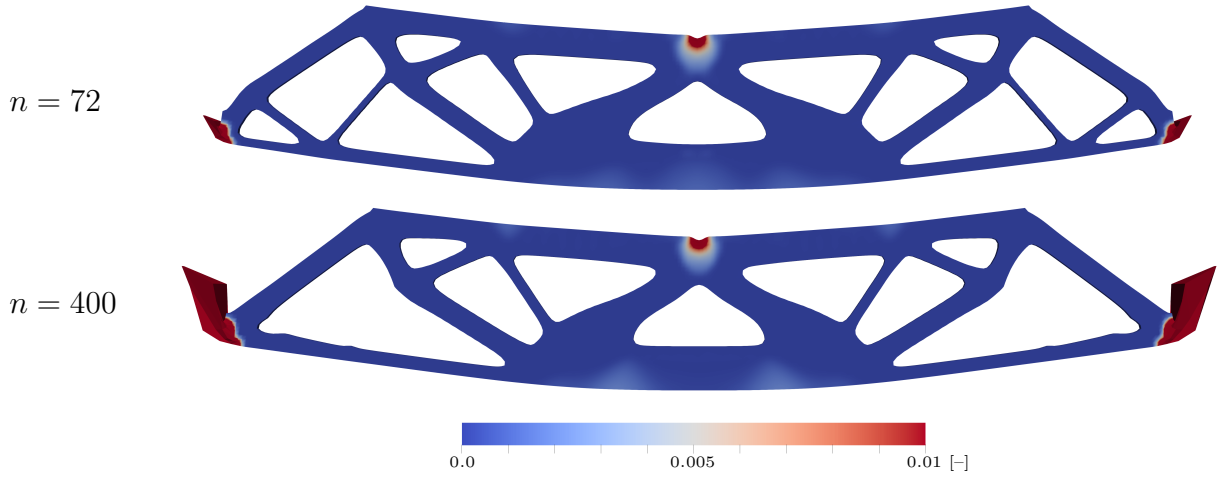


Figure 33: Yielding of the force-controlled quasi 2D MBB beam with 9600 elements when only the corner nodes are supported. The structure is colored with the plastic strains ϵ_{VM}^P and the deformed state is scaled with the factor 15

the L-shaped cantilever in Fig. 34. Here, the stiffness is analyzed for various intensities of the external load \mathbf{f}^* . Similarly, the various intensities of the external force have an influence on the magnitude of plastic strains and thus on the resulting structure. The respective optimal structures are compared in Fig. 35.

4.2.5 Plastic strains during the optimization process

In Fig. 36, the evolution of the plastic strains ϵ^P during the optimization process is exemplary presented for the coarse quasi 2D cantilever. Here, we employ a force-controlled simulation in which larger deformations occur than for a displacement-controlled simulation, see explanations in Sec. 4.2.4. Consequently, more remarkable rearrangements of plastic deformations are present for force-controlled simulations. Therefore, we set $\mathbf{f}^* = 0.8 \text{ N}$, which represents a high loading. The evolution of plastic strains only takes place in spacial regions of the design space which contain full material, i. e., no plastic strains evolves in void regions. Furthermore, it is worth mentioning that the amount of plastic strains also reduces during the optimization while stiffness increases and thus strains are locally reduced (again). This can be seen when comparing the

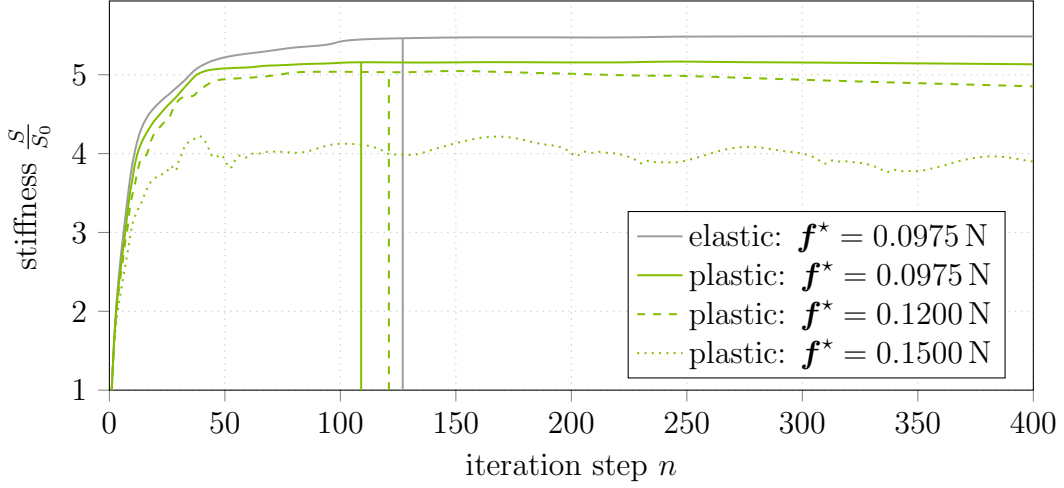


Figure 34: Evolution of stiffness for the force-controlled L-shaped cantilever for various intensities of the external load. The first time that the convergence criterion has been reach is indicated by a vertical line.

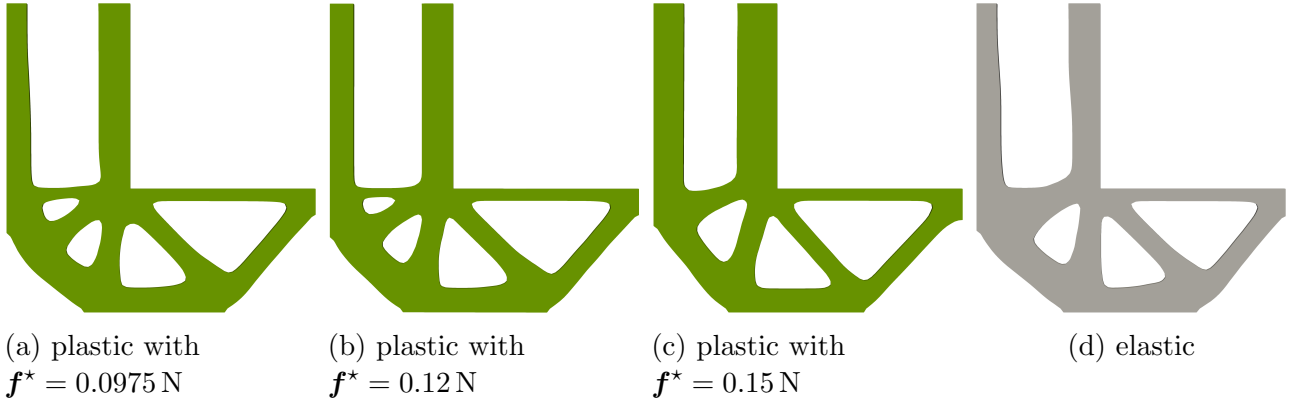


Figure 35: Comparative structure results for various intensities of the external load for force-controlled optimizations for the quasi 2D L-shaped cantilever

iteration steps $n = 72$, $n = 106$ and $n = 190$ in Fig. 36. Therefore, it is a crucial property of the proposed material model to reduce plasticity without dissipation. This proves that the proposed surrogate material model for plasticity without dissipation operates as expected. It is thus possible to consider the plastic strain evolution simply by considering the current strain while avoiding the repeated computation of the entire loading path.

To validate the distribution of plastic strains, the L-shaped cantilever is optimized once again using comparable parameters for the geometry, material and optimization as presented by Xia *et al.* [39]. The geometry dimensions are given in the same ratio (Fig. 14) but with unit length m. Further material and model parameters are given in Tab. 5 and Tab. 6. We

Table 5: Material parameters cf. [39]

Young's module E_0 [MPa]	Poisson's ratio ν [-]	yield stress σ_{exp}^Y [MPa]
75 000	0.3	100

show the distribution of plastic strains on the resulting structures in Fig. 37. Obviously, these larger prescribed displacements result in higher plastic strains. It is worth mentioned that the computed structures and the magnitude of the plastic strains agree to the results by Xia *et al.*

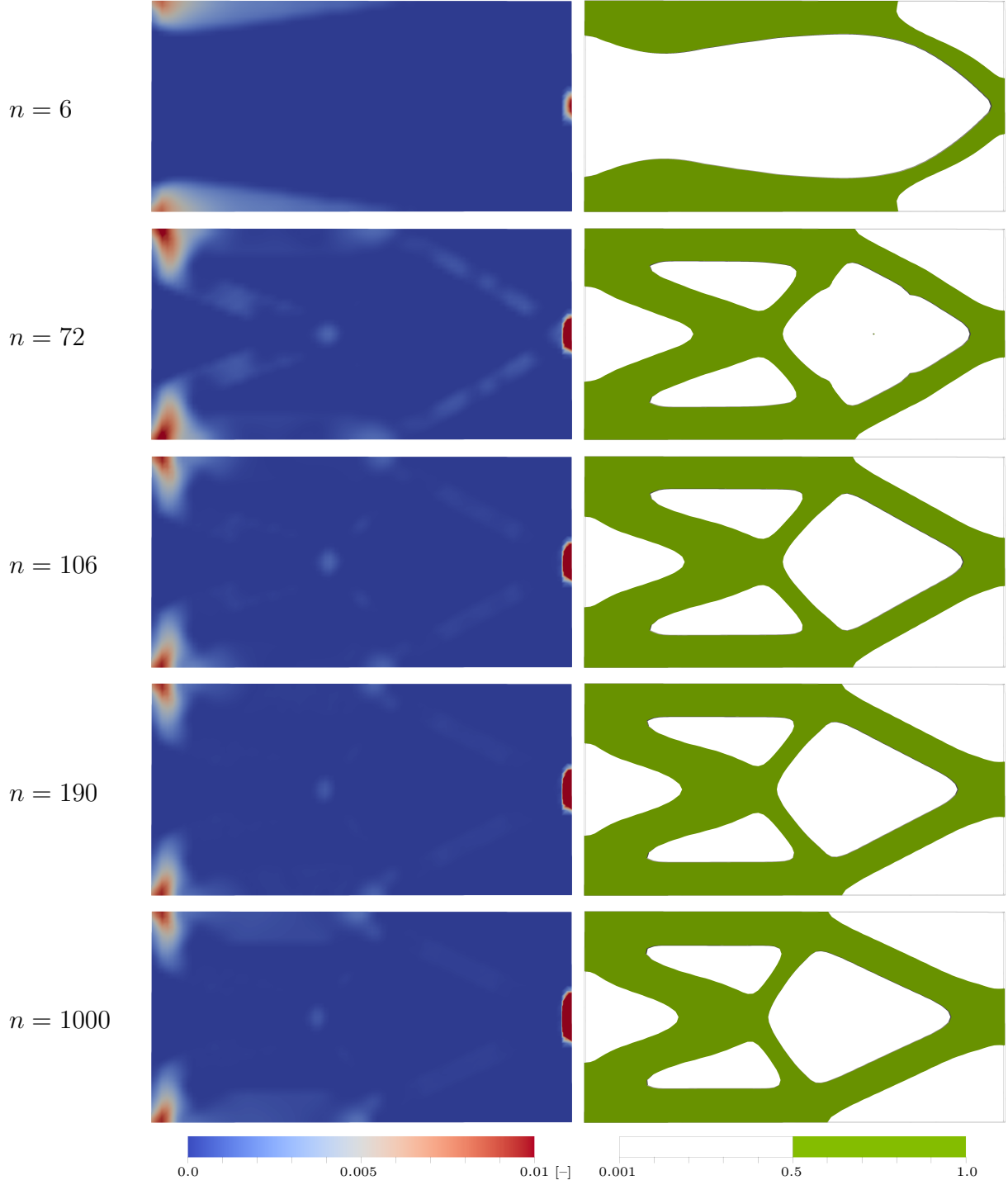


Figure 36: Evolution of plastic strains ε_{VM}^p and topology for various iteration steps n during force-controlled optimization of the quasi 2D cantilever

Table 6: Model parameters cf. [39]

boundary value problem	$\#_{\text{elements}}$	\mathbf{u}^* [mm]	ϱ_0 [–]	η^* [s]	β^* [mm ²]
quasi 2D L-shaped cantilever	6400	8	0.40	15	200
	6400	16	0.40	15	200

in [39].

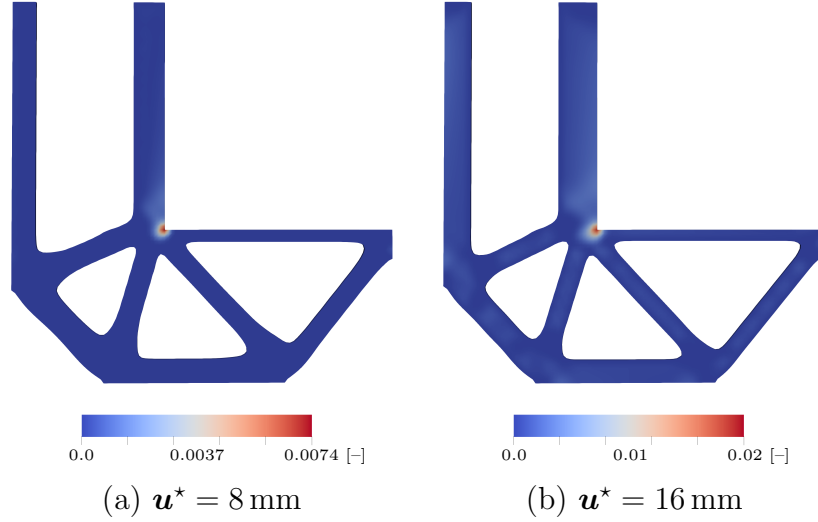


Figure 37: Validation of the distribution of plastic strains ε_{VM}^p of the displacement-controlled quasi 2D L-shaped cantilever by literature results of [39]

4.2.6 Computing time

We present the relative computing times for all examples investigated above in Tab. 7. Here, we scaled the respective runtimes by those needed for the elastic optimization. Interestingly, the optimization including plasticity is not generally consuming much more computation time (runtime & iteration steps): for instance, the plastic simulations converge after only two more iteration steps for the coarse quasi 2D cantilever yielding a time difference of only 1 % as compared to the elastic optimization. Furthermore, the plastic simulations for the 3D cantilever converge after 42 fewer iterations and 19 % fewer runtime compared to the elastic optimization. However, for other cases, the elastic optimization is faster, cf. the clamped beam.

Table 7: Overview of the relative runtimes for the displacement-controlled optimization until convergence. For the fine discretization of the 2D cantilever, convergences was reached according to its definition in Sec. 4.2.3. However, the structure evolution continues for which we mark the reaching of the convergence criterion by $(\cdot)^*$.

boundary value problem	#elements	material model	convergence iteration	relative runtime
quasi 2D MBB beam	2400	plastic	117	1.24
	2400	elastic	96	1.00
	9600	plastic	236	1.43
	9600	elastic	160	1.00
quasi 2D cantilever	3200	plastic	109	1.01
	3200	elastic	107	1.00
	12 800	plastic	$(75)^*$	$(0.57)^*$
	12 800	elastic	133	1.00
quasi 2D L-shaped cantilever	4032	plastic	148	1.17
	4032	elastic	129	1.00
quasi 2D clamped beam	10 000	plastic	283	3.59
	10 000	elastic	76	1.00
3D cantilever	41 472	plastic	171	0.81
	41 472	elastic	213	1.00

Along with the total runtimes, the computation time needed per iteration step is another point of interest. We present for all examples this number and scale it by the number of finite elements used for the respective boundary value problem. The results are collected in Fig. 38.

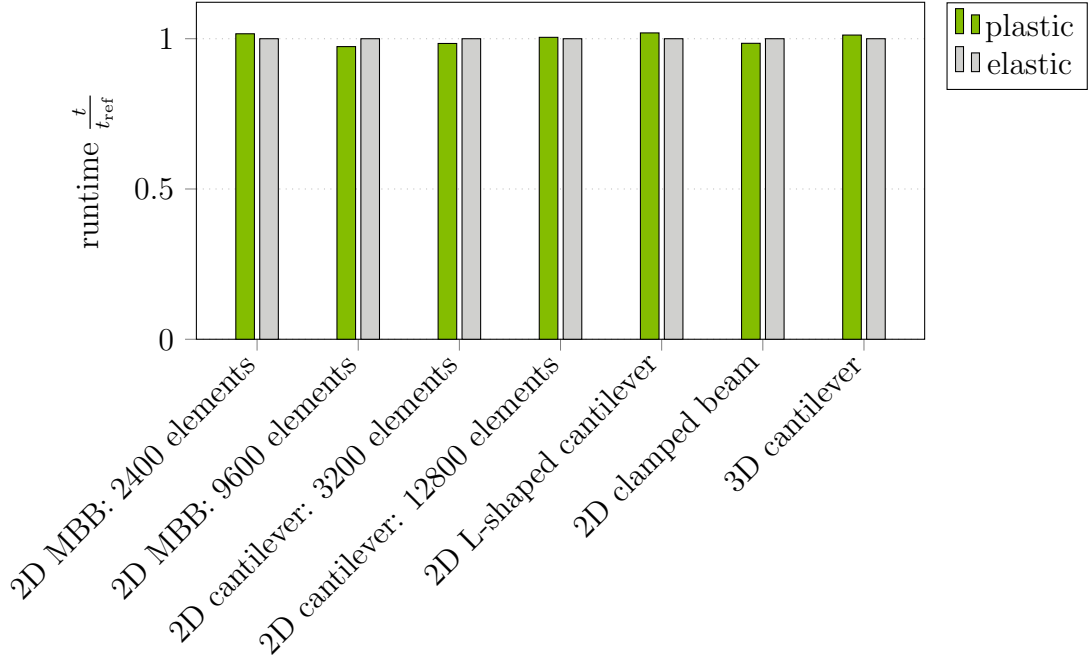


Figure 38: Relative runtimes per iteration step and scaled by the number of elements for each displacement-controlled boundary value problem

Here, we define a reference runtime given by each computation time of the corresponding elastic optimization. Comparable averaged runtimes were observed for all boundary value problems we investigated. It is of particular importance that the plastic simulations not always needed more relative runtime per iteration step than the elastic counterpart. However, a higher number of iteration steps may be needed for the plastic optimization than for the elastic one for convergence, see Tab. 7.

In total, we can conclude that a great advantage of the thermodynamic topology optimization including plasticity is given by a minimum extra effort of computing time; for some simulations, the total computation time is even less than for the reference elastic optimization. The reason for this property is indeed the dissipation-free formulation of our material model and thus, the removed need to resolve the path-dependence.

4.3 Comparison to classical elasto-plastic simulations

An important difference of our novel surrogate model for dissipation-free plasticity to classical elasto-plastic material models is that we do not formulate our model by using an ordinary differential equation. Consequently, path-dependence, as intended, is excluded in our model. Of course, there exists no proof that the different formulations, ODE for classical models vs. algebraic equation for our model, give same results even when only the loading case is considered for which we demand a similar material behavior. To investigate the quality of our novel model in this regard, we discuss the results for the MBB beam and the L-shaped cantilever in this section.

To this end, we use the distribution of the density at the last iteration step and apply for this boundary value problem with inhomogeneous material properties (due to the scaling of the elastic constants with the density χ^3) a classical elasto-plastic simulation. The simulations are carried

out in a displacement-controlled fashion, we hence prescribe the final displacement resulting from the optimization with traction boundary conditions and ramp the maximum displacement up over 100 iteration steps. The results are given in Fig. 39 for the fine MBB beam and for the L-shaped cantilever in Fig. 40. We both show the distribution of plastic strains at the last optimization

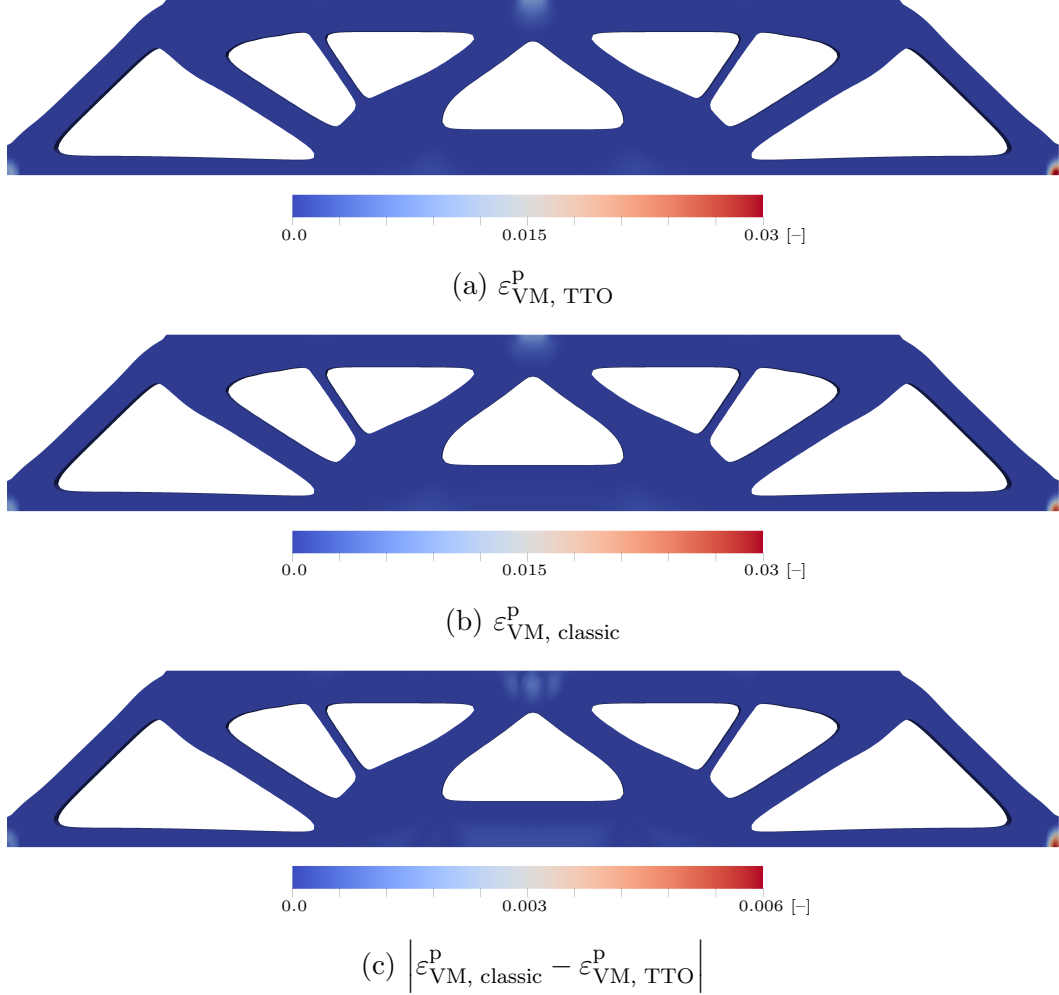


Figure 39: Comparison of the distribution of plastic strains of the displacement-controlled quasi MBB beam with 9600 elements

step (whose density distribution served as input for the elasto-plastic simulation) and the for the elasto-plastic simulation. Furthermore, the absolute value of the difference is plotted. The magnitude of plastic strains corresponds to the chosen external loading, as mentioned before. We see that the maximum deviation is a plastic strain of approximately 0.6 % for the MBB beam (with a maximum plastic strain of 3 %) and 0.06 % for the L-shaped cantilever (with a maximum plastic strain of 0.5 %). It is remarkable that in the critical notch of the L-shaped cantilever the absolute difference of plastic strains is only about 0.02 %. Considering the mathematical difference of the two models, the difference of computed plastic strain is unexpectedly low. It should be noted that the proposed surrogate model overestimates the plastic strains which renders the deviations from a classical plasticity model acceptable.

Moreover, we compare the distribution of the von Mises stress and show the relative difference related to the maximum stress $\sigma_{\text{exp}}^{\text{Y}} = 300$ MPa. This is presented for the MBB beam in Fig. 41 and for the L-shaped cantilever in Fig. 42. The largest stress differences are detected at the same locations where the largest differences in the plastic strains are present. The maximum deviation of stresses are 10 % for the MBB beam and 4.3 % for the L-shaped cantilever. Zhao

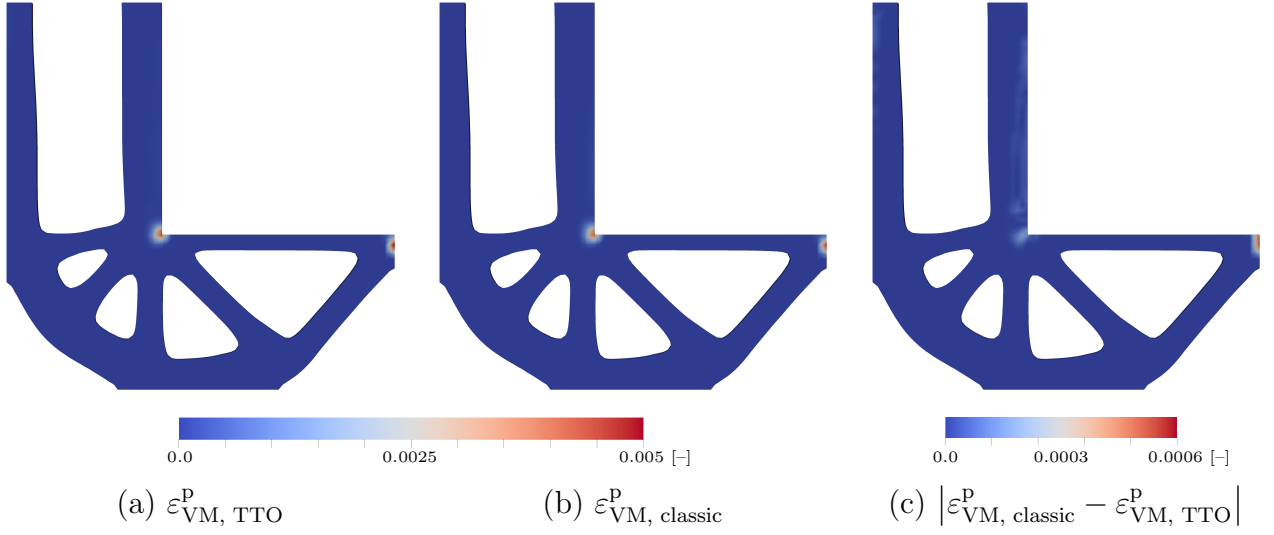


Figure 40: Comparison of the distribution of plastic strains of the displacement-controlled quasi 2D L-shaped cantilever

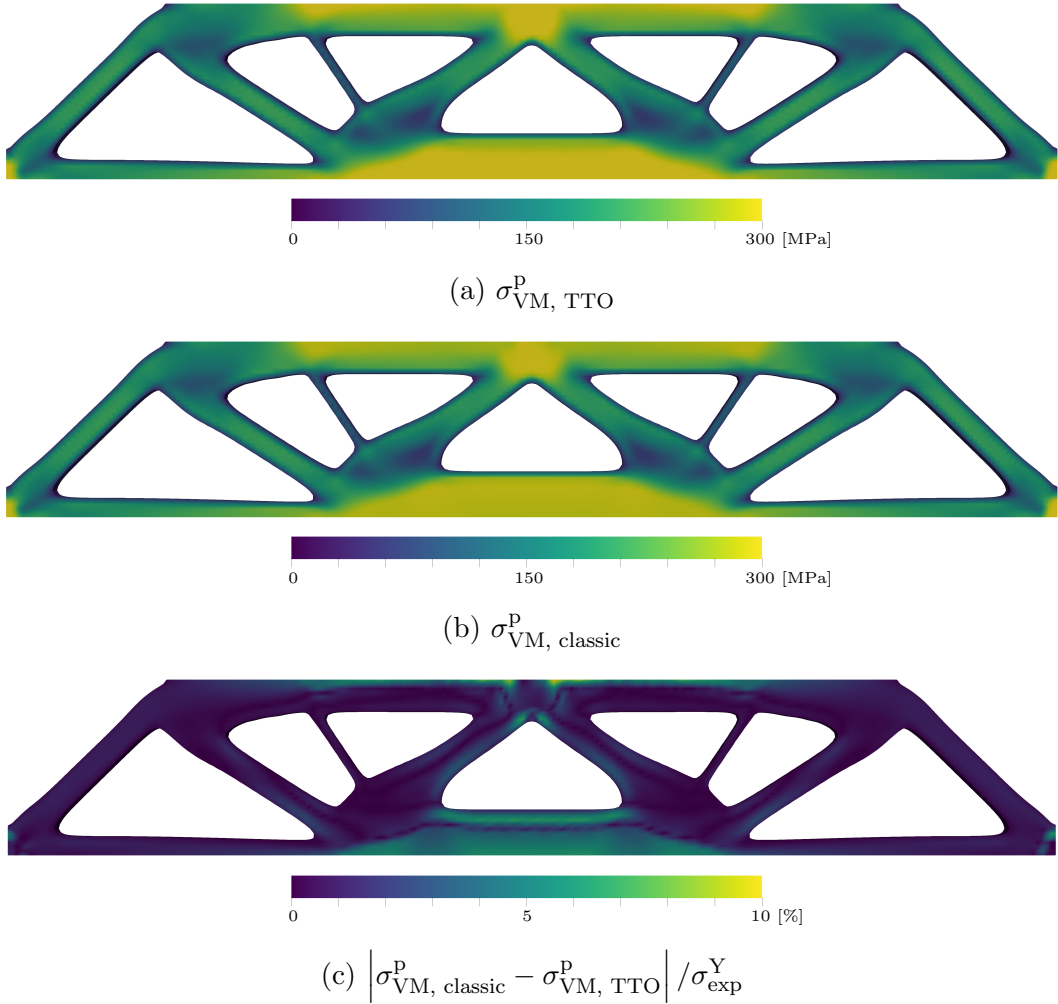


Figure 41: Comparison of the distribution of stress of the displacement-controlled quasi MBB beam with 9600 elements

et al. [42] presents a similar comparison accounting for their non-linear elastic surrogate model and a classical von Mises plasticity where significant differences are obvious. In contrast, the

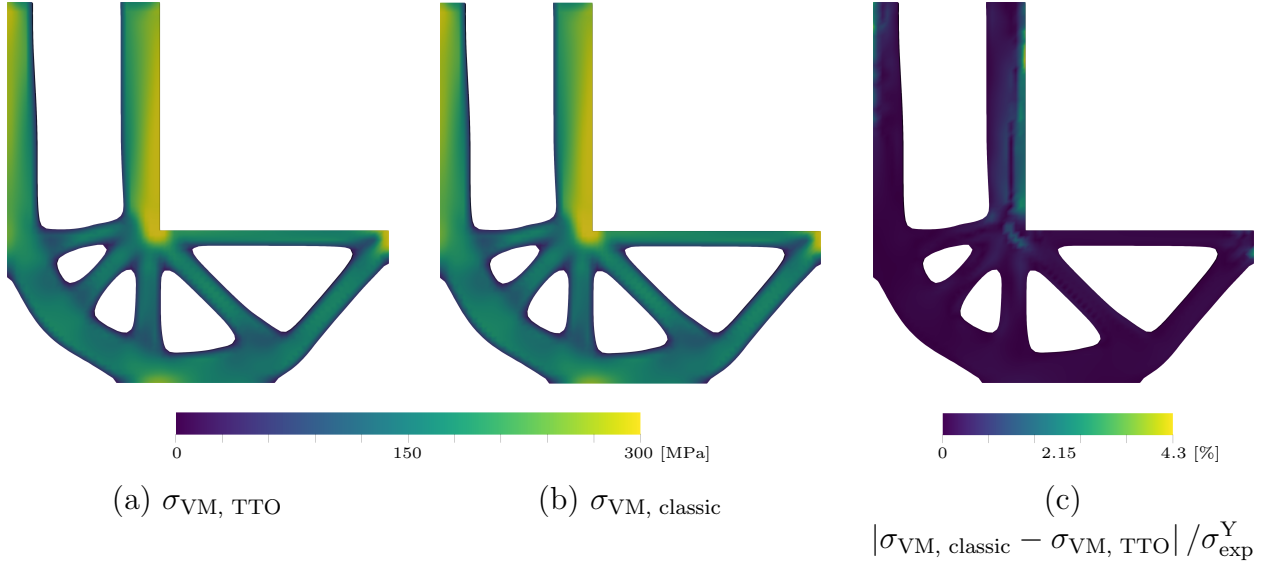


Figure 42: Comparison of the distribution of stress of the displacement-controlled quasi 2D L-shaped cantilever

differences in the stress are rather small with our surrogate material model. Hence, we can conclude that our approach to thermodynamic topology optimization including plasticity indeed considers the physical material behavior with sufficient accuracy.

5 Conclusion

A novel approach to the thermodynamic topology optimization including plasticity was presented. To avoid the computation of a complete load path for estimating the plastic strain state in every optimization step, a novel surrogate material model was developed. To this end, the model was constructed to be dissipation-free such that the plastic strains result from pure energy minimization. The resultant system of governing equations followed as stationarity conditions from an extended Hamilton functional. The system comprised the field equations for the displacements and the density variable, and an algebraic equation for the plastic strains. For the numerical implementation, we employed the neighbored element method for solving the weak form of the balance of linear momentum and the strong form of the evolution equation for the density variable. For the solution of the algebraic equation for the plastic strains, a transformation in the eigenspace has proven beneficial. The numerical treatment was complemented by explicit time-stepping and an operator split. We presented both a material point investigation to demonstrate the general functionality of the novel material model and various finite boundary value problems for displacement-controlled and selected force-controlled simulations. Significant deviations between optimized structures for purely elastic materials and the surrogate model for plastic deformations could be detected. Furthermore, the non-linear character of the plastic structures was observed by a clear dependence on the magnitude of the external forces. During the optimization process, our surrogate material model allows both to predict the microstructural state both for increasing and decreasing strain states due to topology optimization: the plastic strains always correspond to a state evolved during pure loading as is the case for the optimized component during real application. This was confirmed by investigations of the evolution of plastic strain in the course of optimization by comparisons to classical elasto-plastic simulations. Thereby, also the stress state was compared. A remarkable numerical advantage is a computation runtime for the optimization including plasticity is comparable to that for an

elastic optimization. Finally, our method offers a fast and meaningful formulation of topology optimization to take into account the complex and important microstructural behavior in terms of plastic deformations.

Acknowledgment

We highly acknowledge the funding of this research by the Deutsche Forschungsgemeinschaft (DFG, German Research Foundation) through the project grant JU 3096/2-1.

A Derivation of the surrogate material model

From the stationarity condition $(13)_2$, the Lagrange parameters λ_σ and λ_V need to be computed. Therefore, let us reformulate (24) such that we can compute λ_σ and λ_V analytically. To this end, both sides of (24) are double contracted by the deviator operator \mathbb{P} from the left hand side. This yields

$$(54) \quad \mathbb{P} : \boldsymbol{\sigma} = \boldsymbol{\sigma}^{\text{dev}} = -\lambda_\sigma \frac{\boldsymbol{\sigma}^{\text{dev}}}{\|\boldsymbol{\sigma}^{\text{dev}}\|} : \mathbb{P} : \chi^3 \mathbb{E}_0$$

where we used $\mathbb{P} : \boldsymbol{\sigma}^{\text{dev}} = \boldsymbol{\sigma}^{\text{dev}}$ and $\mathbb{P} : \mathbf{I} = \mathbf{0}$. Furthermore, it holds $\boldsymbol{\sigma}^{\text{dev}} : \mathbb{P} : \chi^3 \mathbb{E}_0 = \boldsymbol{\sigma}^{\text{dev}} : \chi^3 \mathbb{E}_0$. Afterwards, we double contract both sides by the stress deviator from the right-hand side, yielding

$$(55) \quad \boldsymbol{\sigma}^{\text{dev}} : \boldsymbol{\sigma}^{\text{dev}} = \|\boldsymbol{\sigma}^{\text{dev}}\|^2 = -\lambda_\sigma \frac{\boldsymbol{\sigma}^{\text{dev}}}{\|\boldsymbol{\sigma}^{\text{dev}}\|} : \chi^3 \mathbb{E}_0 : \boldsymbol{\sigma}^{\text{dev}}.$$

Finally, we insert the constraint $\|\boldsymbol{\sigma}^{\text{dev}}\| = r$ which gives us

$$(56) \quad \lambda_\sigma = -\frac{r^3}{\boldsymbol{\sigma}^{\text{dev}} : \chi^3 \mathbb{E}_0 : \boldsymbol{\sigma}^{\text{dev}}}.$$

To compute the Lagrange parameter λ_V , we double contract (24) with \mathbf{I} from the right-hand side. This results in

$$(57) \quad \begin{aligned} \text{tr } \boldsymbol{\sigma} &= -\lambda_\sigma \frac{\boldsymbol{\sigma}^{\text{dev}}}{r} : \mathbb{P} : \chi^3 \mathbb{E}_0 : \mathbf{I} + 3\lambda_V \\ \Rightarrow \quad \lambda_V &= \frac{1}{3} \text{tr } \boldsymbol{\sigma} + \frac{\lambda_\sigma}{3r} \boldsymbol{\sigma}^{\text{dev}} : \mathbb{P} : \chi^3 \mathbb{E}_0 : \mathbf{I} = \frac{1}{3} \text{tr } \boldsymbol{\sigma} - \frac{r^2}{3} \frac{\boldsymbol{\sigma}^{\text{dev}} : \mathbb{P} : \mathbb{E}_0 : \mathbf{I}}{\boldsymbol{\sigma}^{\text{dev}} : \mathbb{E}_0 : \boldsymbol{\sigma}^{\text{dev}}}. \end{aligned}$$

Then, we finally find

$$(58) \quad \begin{aligned} & -\boldsymbol{\sigma}^{\text{dev}} + r^2 \frac{\boldsymbol{\sigma}^{\text{dev}} : \mathbb{E}_0}{\boldsymbol{\sigma}^{\text{dev}} : \mathbb{E}_0 : \boldsymbol{\sigma}^{\text{dev}}} - \frac{r^2}{3} \frac{\boldsymbol{\sigma}^{\text{dev}} : \mathbb{E}_0 : \mathbf{I}}{\boldsymbol{\sigma}^{\text{dev}} : \mathbb{E}_0 : \boldsymbol{\sigma}^{\text{dev}}} \mathbf{I} = \mathbf{0} \\ \Leftrightarrow & \quad -\boldsymbol{\sigma}^{\text{dev}} + \frac{r^2}{\boldsymbol{\sigma}^{\text{dev}} : \mathbb{E}_0 : \boldsymbol{\sigma}^{\text{dev}}} \left(\boldsymbol{\sigma}^{\text{dev}} : \mathbb{E}_0 - \frac{1}{3} \boldsymbol{\sigma}^{\text{dev}} : \mathbb{E}_0 : \mathbf{I} \mathbf{I} \right) = \mathbf{0} \\ \Leftrightarrow & \quad -\mathbb{P} : \boldsymbol{\sigma} + \frac{r^2}{\boldsymbol{\sigma}^{\text{dev}} : \mathbb{E}_0 : \boldsymbol{\sigma}^{\text{dev}}} \mathbb{P} : (\boldsymbol{\sigma}^{\text{dev}} : \mathbb{E}_0) = \mathbf{0} \\ \Leftrightarrow & \quad \mathbb{P} : \left(-\boldsymbol{\sigma} + \frac{r^2}{\boldsymbol{\sigma}^{\text{dev}} : \mathbb{E}_0 : \boldsymbol{\sigma}^{\text{dev}}} \boldsymbol{\sigma}^{\text{dev}} : \mathbb{E}_0 \right) = \mathbf{0} \end{aligned}$$

which constitutes as the governing equation for the plastic strains.

B Derivation of the yield function

For the transformation of the yield function to be formulated in terms of strains, let us first investigate the computation of the threshold value r based on experimental data. Usually, a tension test is employed to determine the strength of a material. Here, the stress state

$$(59) \quad \boldsymbol{\sigma}^Y = \sigma_{\text{exp}}^Y \begin{pmatrix} 1 & 0 & 0 \\ 0 & 0 & 0 \\ 0 & 0 & 0 \end{pmatrix}$$

is present with the stress deviator

$$(60) \quad \boldsymbol{\sigma}^{\text{dev},Y} = \mathbb{P} : \boldsymbol{\sigma}^Y = \sigma_{\text{exp}}^Y \begin{pmatrix} \frac{2}{3} & 0 & 0 \\ 0 & -\frac{1}{3} & 0 \\ 0 & 0 & -\frac{1}{3} \end{pmatrix} .$$

Consequently, the norm of the stress deviator for the tensile test yields

$$(61) \quad \|\boldsymbol{\sigma}^{\text{dev},Y}\| = \sqrt{\frac{2}{3}} \sigma_{\text{exp}}^Y = r$$

which allows us to compute the value of the dissipation parameter r based on an experimentally determined yield stress. The strain state related to the stress state for yielding in the tensile test of isotropic materials is given as

$$(62) \quad \boldsymbol{\varepsilon}^Y = \varepsilon_{\text{exp}}^Y \tilde{\boldsymbol{\varepsilon}}_{\text{tens}} \quad \text{where} \quad \tilde{\boldsymbol{\varepsilon}}_{\text{tens}} = \begin{pmatrix} 1 & 0 & 0 \\ 0 & -\nu & 0 \\ 0 & 0 & -\nu \end{pmatrix} .$$

Here, the quantity $\tilde{\boldsymbol{\varepsilon}}_{\text{tens}}$ represents the normalized strain during a tensile test. It can be modified accordingly for anisotropic materials. This expression can be inserted into the formula for the stress, resulting in

$$(63) \quad \boldsymbol{\sigma}^Y = \chi^3 \mathbb{E}_0 : \boldsymbol{\varepsilon}^Y$$

such that we arrive at the following formulation for the indicator function when the yield limit is reached:

$$(64) \quad \Phi = \|\boldsymbol{\sigma}^{\text{dev}}\| - r = \|\mathbb{P} : \chi^3 \mathbb{E}_0 : \boldsymbol{\varepsilon}^Y\| - r = 0 .$$

Therefrom, we obtain (28).

C Finite element method according to Ferrite

A possible implementation of the thermodynamic topology optimization including plasticity by use of the Ferrite package [1] and the tensors package [4] is presented in the Alg. 2 and Alg. 3.

Algorithm 2 Finite element implementation in Ferrite [1]

while true do

for each $element \in mesh$ **do** ▷ repeat for each element

call `reinit!(mesh, elementvalues)` ▷ update element values

for each $ip \in element$ **do** ▷ repeat for each integration point

[illegible]

```
compute  $\sigma$  and  $\epsilon^p$                                 ▷ do material update
```

compute $\Omega^* = \text{getdetJdV}(\text{elementvalues}, ip)$ \triangleright weighted volume fraction

for i do ▷ repeat for all shape functions

```
compute  $\mathbf{B}^T = \text{shape\_symmetric\_gradient}(elementvalues, ip, i)$   

▷ derivative of shape functions
```

```
compute  $\mathbf{r}_e[i] += (\mathbf{B}^\top : \boldsymbol{\sigma}) \Omega^*$   $\triangleright$  build element residual vector
```

[illegible]

compute $\mathbf{B} = \text{shape_symmetric_gradient}(\text{elementvalues}, ip, j)$
 \triangleright derivative of base shape function

compute $\mathbf{K}_e[i, j] += (\mathbf{B}^T : \boldsymbol{\sigma} : \mathbf{B}) \Omega^*$ \triangleright build element stiffness matrix

end for

end for

compute $\mathbf{r}_e = \mathbf{r}_e - \mathbf{f}_{e,\text{ext}}$	▷ correct element residual vector by subtracting the external forces
---	---

end for

Algorithm 3 Continuation of the finite element method in Ferrite [1]

call assemble!(<i>assembler</i> , \mathbf{K}_e , \mathbf{r}_e)	▷ assemble element results to global stiffness matrix and residual vector
end for	
call apply_zero!(\mathbf{K} , \mathbf{r} , <i>constraints</i>)	▷ apply boundary conditions
if $\ \mathbf{r}\ < \text{tol}$ then break	
end if	▷ check convergence criterion
update $\mathbf{u}_{i+1} = \mathbf{u}_i - \frac{\mathbf{r}}{\mathbf{K}}$	▷ update displacement vector
update $i = i + 1$	▷ update Newton iteration
end while	

References

- [1] Ferrite (previous JuAFEM) (Julia package), <https://github.com/ferrite-fem/ferrite.jl>.
- [2] Julia programming language, www.julialang.org.
- [3] Paraview, www.paraview.org.
- [4] Tensors (Julia package), <https://github.com/ferrite-fem/tensors.jl>.
- [5] Ryan Alberdi and Kapil Khandelwal. Topology optimization of pressure dependent elasto-plastic energy absorbing structures with material damage constraints. *Finite Elements in Analysis and Design*, 133:42–61, 2017.
- [6] Oded Amir. Stress-constrained continuum topology optimization: a new approach based on elasto-plasticity. *Struct Multidisc Optim*, 55:1797–1818, 2016.
- [7] Alexander Bartels, Patrick Kurzeja, and Jörn Mosler. Cahn–hilliard phase field theory coupled to mechanics: Fundamentals, numerical implementation and application to topology optimization. *Computer Methods in Applied Mechanics and Engineering*, 383:113918, 2021.
- [8] M. P. Bendsøe. Optimal shape design as a material distribution problem. *Structural Optimization*, 1:193–202, 1989.
- [9] M. P. Bendsøe and O. Sigmund. *Topology Optimization: Theory, Methods, and Applications*. Springer-Verlag Berlin Heidelberg, 2003.
- [10] Matteo Bruggi and Pierre Duysinx. Topology optimization for minimum weight with compliance and stress constraints. *Struct Multidisc Optim*, 46:369–384, 2012.
- [11] T. E. Bruns, O. Sigmund, and D. A. Tortorelli. Numerical methods for the topology optimization of structures that exhibit snap-through. *International Journal for Numerical Methods in Engineering*, 55(10):1215–1237, 2002.

- [12] P. Duysinx and M. P. Bendsøe. Topology optimization of continuum structures with local stress constraints. *International Journal for Numerical Methods in Engineering*, 43:1453–1478, 1999.
- [13] Pierre Duysinx. Topology optimization with different stress limits in tension and compression. *Third World Congress of Structural and Multidisciplinary Optimization (WCSMO3)*, 1999.
- [14] Felix Fritzen, Liang Xia, Matthias Leuschner, and Piotr Breitkopf. Topology optimization of multiscale elastoviscoplastic structures. *International Journal for Numerical Methods in Engineering*, 106:430–453, 2016.
- [15] Georgios Gaganelis, Dustin Roman Jantos, Peter Mark, and Philipp Junker. Tension/compression anisotropy enhanced topology design. *Structural and Multidisciplinary Optimization*, 59(6):2227–2255, 2019.
- [16] Lothar Harzheim. Strukturoptimierung. *Harri Deutsch, Frankfurt*, 2008.
- [17] Dustin R. Jantos, Klaus Hackl, and Philipp Junker. An accurate and fast regularization approach to thermodynamic topology optimization. *International Journal for Numerical Methods in Engineering*, 117(9):991–1017, 2019.
- [18] Dustin Roman Jantos, Christopher Riedel, Klaus Hackl, and Philipp Junker. Comparison of thermodynamic topology optimization with simp. *Continuum Mechanics and Thermodynamics*, 31(2):521–548, 2019.
- [19] P. Junker, J. Makowski, and K. Hackl. The principle of the minimum of the dissipation potential for non-isothermal processes. *Continuum Mechanics and Thermodynamics*, 26(3):259–268, 2014.
- [20] Philipp Junker and Daniel Balzani. An extended hamilton principle as unifying theory for coupled problems and dissipative microstructure evolution. *Continuum Mechanics and Thermodynamics*, page accepted for publication, 2021.
- [21] Philipp Junker and Daniel Balzani. A new variational approach for the thermodynamic topology optimization of hyperelastic structures. *Computational Mechanics*, (67):455–480, 2021.
- [22] Philipp Junker and Klaus Hackl. A variational growth approach to topology optimization. *Structural and Multidisciplinary Optimization*, 52(2):293–304, 2015.
- [23] Lei Li, Guodong Zhang, and Kapil Khandelwal. Topology optimization of energy absorbing structures with maximum damage constraint. *International Journal for Numerical Methods in Engineering*, 112:737–775, 2017.
- [24] Quantian Luo and Liyong Tong. An algorithm for eradicating the effects of void elements on structural topology optimization for nonlinear compliance. *Structural and Multidisciplinary Optimization*, 53(4):695–714, 2016.
- [25] Yangjun Luo and Zhan Kang. Topology optimization of continuum structures with drucker–prager yield stress constraints. *Computers and Structures*, 90–91:65–75, 2012.
- [26] K. Maute, S. Schwarz, and E. Ramm. Adaptive topology optimization of elastoplastic structures. *Structural Optimization*, 15:81–91, 1998.

- [27] P. B. Nakshatrala and D. A. Tortorelli. Topology optimization for effective energy propagation in rate-independent elastoplastic material systems. *Computer Methods in Applied Mechanics and Engineering*, 295:305–326, 2015.
- [28] Henryk Petryk. Incremental energy minimization in dissipative solids. *Comptes Rendus Mecanique*, 331(7):469–474, 2003.
- [29] Henryk Petryk. Thermodynamic conditions for stability in materials with rate-independent dissipation. *Philosophical Transactions of the Royal Society A: Mathematical, Physical and Engineering Sciences*, 363(1836):2479–2515, 2005.
- [30] Henryk Petryk. *Material instabilities in elastic and plastic solids*, volume 414. Springer, 2014.
- [31] Henryk Petryk and Stanisław Stupkiewicz. Modelling of microstructural evolution on complex paths of large plastic deformation: Dedicated to prof. dr. fd fischer on the occasion of his 70th birthday. *International journal of materials research*, 103(3):271–277, 2012.
- [32] Henryk Petryk and Klaus Thermann. On discretized plasticity problems with bifurcations. *International journal of solids and structures*, 29(6):745–765, 1992.
- [33] Axel Schumacher. *Optimierung mechanischer Strukturen: Grundlagen und industrielle Anwendungen*. Springer, 2013.
- [34] Ole Sigmund and Kurt Maute. Topology optimization approaches. *Structural and Multidisciplinary Optimization*, 48(6):1031–1055, 2013.
- [35] C. Swan and I. Kosaka. Voigt–reuss topology optimization for structures with nonlinear material behaviors. *International Journal for Numerical Methods in Engineering*, 40:3785–3814, 1998.
- [36] Andreas Vogel and Philipp Junker. Adaptive thermodynamic topology optimization. *Structural and multidisciplinary optimization*, accepted for publication, 2020.
- [37] Mathias Wallin, Viktor Jönsson, and Eric Wingren. Topology optimization based on finite strain plasticity. *Struct Multidisc Optim*, 54:783–793, 2016.
- [38] Peter Wriggers. *Nonlinear finite element methods*. Springer Science & Business Media, 2008.
- [39] Liang Xia, Felix Fritzen, and Piotr Breitkopf. Evolutionary topology optimization of elastoplastic structures. *Structural and Multidisciplinary Optimization*, 55:569–581, 2017.
- [40] K. Yuge and N. Kikuchi. Optimization of a frame structure subjected to a plastic deformation. *Structural Optimization*, 10:197–208, 1995.
- [41] Tuo Zhao, Eduardo N. Lages, Adeildo S. Ramos Jr., and Glaucio H. Paulino. Topology optimization considering the drucker–prager criterion with a surrogate nonlinear elastic constitutive model. *Structural and Multidisciplinary Optimization*, 62:3205–3227, 2020.
- [42] Tuo Zhao, Adeildo S. Ramos Jr., and Glaucio H. Paulino. Material nonlinear topology optimization considering the von mises criterion through an asymptotic approach: Max strain energy and max load factor formulations. *International Journal for Numerical Methods in Engineering*, 118:804–828, 2019.